Zonal flow regimes in rotating anelastic spherical shells: an application to giant planets

T. Gastine[a,∗], J. Wicht[a], J.M. Aurnou[b]

[a]*Max Planck Institut für Sonnensytemforschung, Max Planck Strasse 2, 37191 Katlenburg Lindau, Germany*
[b]*Department of Earth and Space Sciences, University of California, Los Angeles, CA, 90095-1567 USA*

Abstract

The surface zonal winds observed in the giant planets form a complex jet pattern with alternating prograde and retrograde direction. While the main equatorial band is prograde on the gas giants, both ice giants have a pronounced retrograde equatorial jet.

We use three-dimensional numerical models of compressible convection in rotating spherical shells to explore the properties of zonal flows in different regimes where either rotation or buoyancy dominates the force balance. We conduct a systematic parameter study to quantify the dependence of zonal flows on the background density stratification and the driving of convection.

In our numerical models, we find that the direction of the equatorial zonal wind is controlled by the ratio of the global-scale buoyancy force and the Coriolis force. The prograde equatorial band maintained by Reynolds stresses is found in the rotation-dominated regime. In cases where buoyancy dominates Coriolis force, the angular momentum per unit mass is homogenised and the equatorial band is retrograde, reminiscent to those observed in the ice giants. In this regime, the amplitude of the zonal jets depends on the background density contrast with strongly stratified models producing stronger jets than comparable weakly stratified cases. Furthermore, our results can help to explain the transition between solar-like (i.e. prograde at the equator) and the "anti-solar" differential rotations (i.e. retrograde at the equator) found in anelastic models of stellar convection zones.

In the strongly stratified cases, we find that the leading order force balance can significantly vary with depth. While the flow in the deep interior is dominated by rotation, buoyancy can indeed become larger than Coriolis force in a thin region close to the surface. This so-called "transitional regime" has a visible signature in the main equatorial jet which shows a pronounced dimple where flow amplitudes notably decay towards the equator. A similar dimple is observed on Jupiter, which suggests that convection in the planet interior could possibly operate in this regime.

Keywords: Atmospheres dynamics, Jupiter interior, Saturn interior, Uranus interior, Neptune interior

1. Introduction

Surface zonal jets on the giant planets Jupiter, Saturn, Uranus and Neptune have been investigated since the 1970's by tracking cloud features (e.g. Ingersoll, 1990). On each planet, these zonal winds form a differential rotation profile with alternating prograde (i.e. eastward) and retrograde (i.e. westward) flows.

On both gas giants, a strong eastward equatorial jet is flanked by multiple weaker alternating zonal winds (10-20 m.s^{-1}). Jupiter's equatorial jet extends roughly between ±20° latitude reaching a maximum velocity around 150 m.s^{-1} (Porco et al., 2003; Vasavada and Showman, 2005). Saturn's equatorial jet is fiercer and wider with a maximum flow amplitude of 450 m.s^{-1} and extension of ±35° latitude (Porco et al., 2005).

The zonal wind profiles of Uranus and Neptune are quite different. One broad retrograde equatorial jet is flanked by only two strong prograde jets at higher latitudes. On Uranus, this equatorial sub-rotation extends between ±30° latitude and reaches 100 m.s^{-1} (Hammel et al., 2005); it extends over ±50° latitudes and reaches 400 m.s^{-1} on Neptune (Sromovsky et al., 1993).

Two competing categories of models try to explain the observed zonal winds structure. In the "shallow-forcing" scenario, zonal winds are driven by injection of turbulence via different types of physical forcings at the stably-stratified cloud level (e.g., latent heat release, solar radiation, moist convection). These models successfully reproduce an alternating zonal flow pattern similar to those observed in giant planets (e.g. Williams, 1978; Cho and Polvani, 1996). Although many earlier shallow models predict a similar westward equatorial zonal flow for all four giant planets, recent studies show that these models can also replicate the equatorial zonal flows of the four giant planets via the inclusion of an additional forcing mechanism such as water vapor condensation (Lian and Showman, 2010) or via enhanced radiative damping (Scott and Polvani, 2008; Liu and Schneider, 2011).

In the "deep-forcing" scenario, zonal winds are maintained by deep-seated convection. The increasing electrical conductivity in the deep-interior of the giant planets (Nettelmann et al., 2008; French et al., 2012) goes along with stronger Lorentz forces that are thought to prevent the strong zonal winds to penetrate deep into the molecular layer. Liu et al. (2008) therefore argued that the zonal winds must be confined in a thin upper layer (0.85 R_S and 0.96 R_J), since deep jets extending over the whole molecular envelope would lead to Ohmic dissipa-

tion that would exceed the planetary luminosity. More recent dynamo models by Heimpel and Gómez Pérez (2011) support the idea that zonal flows would maybe reach less than half of the distance to the bottom of the molecular layer. These deep models rely on 3-D numerical simulations of rapidly-rotating spherical shells. In rotating convection at moderate convective forcing, convection occurs on long, axially-oriented columns reaching through the whole fluid layer. These well-organized columnar flows generate Reynolds stresses (i.e. statistical correlations between the convective flow components) that drive strong zonal winds (e.g. Busse, 1983, 1994; Plaut et al., 2008; Brown et al., 2008). The typical azimuthally prograde tilt of these convective columns always yields an eastward equatorial jet (e.g. Zhang, 1992; Christensen, 2001; Aurnou and Heimpel, 2004). The direction and the number of jets are consistent with Jupiter's and Saturn's observation provided thin shells and low Ekman numbers are considered (e.g. Heimpel et al., 2005; Heimpel and Aurnou, 2007).

A different zonal flow regime is however found when global-scale buoyancy starts to dominate the Coriolis force. The equatorial zonal flow tends to reverse (e.g. Gilman, 1977; Gilman and Foukal, 1979; Glatzmaier and Gilman, 1982). Responsible for the latter is the turbulent mixing of angular momentum, which may explain the strong retrograde equatorial zonal flow observed on the ice giants (Aurnou et al., 2007).

To further inform the ongoing discussion on the driving mechanisms and the depth of the zonal jets in the giant planets, here we investigate the deep-seated zonal flow perspective and thus compute 3-D global models of convection in spherical shells.

Many of the previous parameter studies have employed the Boussinesq approximation where the density stratification is simply ignored (Christensen, 2002; Aurnou et al., 2007). This is rather dubious in the strongly stratified giant planets where the density contrasts are huge (e.g. Nettelmann et al., 2012a,b). More recent models therefore use the anelastic approximation which allows to incorporate the effects of background stratification while filtering out the fast acoustic waves (e.g. Braginsky and Roberts, 1995; Lantz and Fan, 1999; Brown et al., 2012). In an extensive parameter study, Gastine and Wicht (2012) concentrate on the influence of the density stratification on convection and zonal flows in the rotation-dominated regime (see also Showman et al., 2011). While the density stratification affects the local scales and the amplitude of the convective flow, the mean zonal flows and the global quantities are fairly independent of the density contrast, similar to the results of Jones and Kuzanyan (2009).

Many anelastic and fully compressible models of solar and stellar convection have observed a transition between the solar-like (i.e. eastward equatorial zonal flow) and the so-called "anti-solar" (i.e. westward equatorial zonal flow) differential rotation profiles when buoyancy dominates the force balance (Glatzmaier and Gilman, 1982; Bessolaz and Brun, 2011; Käpylä et al., 2011a). Yet, to date, no systematic parameter study has been made to investigate the influence of density stratification on the transition between the rotation-dominated and the buoyancy-dominated zonal flow regimes.

This is precisely the focus of the present study, which extends the previous Boussinesq study of Aurnou et al. (2007) to anelastic models. To this end, we conduct a systematic parameter study from Boussinesq to strongly stratified models (i.e. $\rho_{\mathrm{bot}}/\rho_{\mathrm{top}} \simeq 150$) and solutions that span the range from weakly to strongly supercritical convection.

In section 2, we present the anelastic formulation and the numerical methods. Section 3 shows the change in convection when the driving is gradually increased from the rotation-dominated to the buoyancy-dominated regime. Section 4 focuses on the zonal flows profiles that develop in the buoyancy-dominated regime. In section 5, we concentrate on the so-called *transitional regime*, a specific feature of strongly stratified anelastic models, before concluding in section 6.

2. Hydrodynamical model and numerical methods

2.1. Governing equations

We consider hydrodynamical simulations of an anelastic ideal gas in a spherical shell rotating at a constant rotation rate Ω about the z-axis. We use a dimensionless formulation of the governing Navier-Stokes equations where the shell thickness $d = r_o - r_i$ is employed as a reference lengthscale and Ω^{-1} as the time unit. Density and temperature are non-dimensionalised using their outer boundaries reference values ρ_{top} and T_{top}. Entropy is expressed in units of Δs, the imposed entropy contrast over the layer. Kinematic viscosity ν, thermal diffusivity κ and heat capacity c_p are assumed to be homogeneous.

Following the anelastic formulations of Gilman and Glatzmaier (1981); Braginsky and Roberts (1995) and Lantz and Fan (1999), the background reference state (denoted with tildes in the following) is hydrostatic and adiabatic. It is defined by $d\tilde{T}/dr = -g/c_p$ and a polytropic gas $\tilde{\rho} = \tilde{T}^m$, m being the polytropic index. As we are interested in the dynamics of the molecular region of giant planets, we assume that the mass is concentrated in the inner part, so that $g \propto 1/r^2$ provides a good approximation (see also Jones and Kuzanyan, 2009; Gastine and Wicht, 2012). Such a gravity profile then leads to the following background temperature profile

$$\tilde{T}(r) = \frac{c_0}{(1-\eta)r} + 1 - c_0 \quad \text{and} \quad \tilde{\rho}(r) = \tilde{T}^m, \quad (1)$$

with

$$c_0 = \frac{\eta}{1-\eta}\left(\exp\frac{N_\rho}{m} - 1\right) \quad \text{with} \quad N_\rho = \ln\frac{\tilde{\rho}(r_i)}{\tilde{\rho}(r_o)}. \quad (2)$$

Here $\tilde{T}$ and $\tilde{\rho}$ are the background temperature and density, $\eta = r_i/r_o$ is the aspect ratio of the spherical shell and N_ρ corresponds to the number of density scale heights over the layer (see also Jones et al., 2011, for the full derivation of the reference state).

In the anelastic approximation, the dimensionless equations that govern convective motions are given by

$$\nabla \cdot (\tilde{\rho}\boldsymbol{u}) = 0, \quad (3)$$

$$\frac{\partial \boldsymbol{u}}{\partial t} + \boldsymbol{u} \cdot \boldsymbol{\nabla} \boldsymbol{u} + 2\boldsymbol{e}_z \times \boldsymbol{u} = -\boldsymbol{\nabla}\frac{p}{\tilde{\rho}} + \mathrm{Ra}^* \frac{r_o^2}{r^2} s\, \boldsymbol{e_r} + \frac{\mathrm{E}}{\tilde{\rho}} \boldsymbol{\nabla} \cdot \mathsf{S}, \quad (4)$$

where $\boldsymbol{u}$, p and s are velocity, pressure and entropy, respectively. S is the traceless rate-of-strain tensor with a constant kinematic viscosity, given by

$$\mathsf{S}_{ij} = 2\tilde{\rho}\left(\mathsf{e}_{ij} - \frac{1}{3}\delta_{ij}\boldsymbol{\nabla} \cdot \boldsymbol{u}\right) \quad \text{with} \quad \mathsf{e}_{ij} = \frac{1}{2}\left(\frac{\partial u_i}{\partial x_j} + \frac{\partial u_j}{\partial x_i}\right), \quad (5)$$

δ_{ij} being the identity matrix. The dimensionless entropy equation reads

$$\tilde{\rho}\tilde{T}\left(\frac{\partial s}{\partial t} + \boldsymbol{u} \cdot \boldsymbol{\nabla} s\right) = \frac{\mathrm{E}}{\mathrm{Pr}} \boldsymbol{\nabla} \cdot \left(\tilde{\rho}\tilde{T}\boldsymbol{\nabla} s\right) + \frac{\mathrm{E}}{\mathrm{Ra}^*}(1-\eta)c_o\, Q_\nu, \quad (6)$$

where Q_ν is the viscous heating contribution given by

$$Q_\nu = 2\tilde{\rho}\left[\mathsf{e}_{ij}\mathsf{e}_{ji} - \frac{1}{3}(\boldsymbol{\nabla} \cdot \boldsymbol{u})^2\right]. \quad (7)$$

In addition to the aspect ratio η and the two parameters involved in the description of the reference state (N_ρ and m), the system of equations (3-6) is governed by three dimensionless parameters, namely, the Ekman number, the Prandtl number and the modified Rayleigh number:

$$\mathrm{E} = \frac{\nu}{\Omega d^2} \; ; \; \mathrm{Pr} = \frac{\nu}{\kappa} \; ; \; \mathrm{Ra}^* = \frac{g_{\mathrm{top}}\Delta s}{c_p \Omega^2 d}, \quad (8)$$

where g_{top} is the gravity at the outer boundary. Ra^* can be related to the standard Rayleigh number $\mathrm{Ra} = g_{\mathrm{top}}d^3\Delta s/c_p\nu\kappa$ with (e.g. Christensen, 2002)

$$\mathrm{Ra}^* = \frac{\mathrm{Ra}\,\mathrm{E}^2}{\mathrm{Pr}}. \quad (9)$$

The definition of Ra^* is based on the global entropy jump over the spherical shell and on the gravity value at the outer boundary. In anelastic models, it is however more appropriate to define a local modified Rayleigh number that encompasses the radial dependence of the background reference state (e.g. Kaspi et al., 2009; Gastine and Wicht, 2012):

$$\mathcal{R}^*(r) = \frac{g}{c_p\Omega^2}\left|\frac{ds_c}{dr}\right|, \quad (10)$$

where s_c is the conduction state entropy, which is the solution of

$$\boldsymbol{\nabla} \cdot \left(\tilde{\rho}\tilde{T}\boldsymbol{\nabla} s_c\right) = 0. \quad (11)$$

As the entropy gradient is inversely proportional to $\tilde{\rho}\tilde{T}$, the value of $\mathcal{R}^*$ can become very large at the surface in the most stratified cases. In these models, convection sets in first in the outermost region (Jones et al., 2009; Gastine and Wicht, 2012). To compare numerical models with different density contrasts, it is either possible to consider a mass-weighted average of $\mathcal{R}^*$ as suggested by Kaspi et al. (2009), or use its value at mid-depth (Unno et al., 1960; Glatzmaier and Gilman, 1981). Table 1 shows that these two definitions lead to very similar results. In the following, we use the modified Rayleigh number

Table 1: Local Rayleigh number at mid-depth and mass-weighted average of $\mathcal{R}^*$ for $\mathrm{Ra}^* = 1$ for different density stratifications.

N_ρ	$\mathcal{R}^*(r_{\mathrm{mid}})$	$\langle \mathcal{R}^* \rangle_\rho$
0.01	1.462	1.534
1	1.563	1.599
3	0.880	0.867
5	0.237	0.245

at mid-depth $\mathcal{R}^*_m \equiv \mathcal{R}^*(r_{\mathrm{mid}})$ to compare our different numerical models.

The first numerical models of rotating convection in spherical shells by Gilman (1977) and Glatzmaier and Gilman (1982) have shown that the physical mechanism responsible of the zonal flow production is sensitive to the relative contribution of buoyancy and Coriolis force in the global-scale force balance. The ratio between these two forces can be related to Ra^* (for the full derivation, see Aurnou et al., 2007) via

$$\frac{\text{Buoyancy}}{\text{Coriolis}} \sim (\mathrm{Ra}^*)^{1/2}. \quad (12)$$

This ratio is commonly referred to as the "convective Rossby number" in the solar and stellar convection communities (e.g. Elliott et al., 2000; Ballot et al., 2007) and in the fluid physics community (e.g. Zhong and Ahlers, 2010). In Boussinesq studies, $\mathrm{Ra}^* \sim 1$ is typically found to be a good proxy to separate the rotation-dominated zonal flow regime (i.e. $\mathrm{Ra}^* \ll 1$) from the buoyancy-dominated flow regime (i.e. $\mathrm{Ra}^* \gg 1$) (Gilman, 1977; Aurnou et al., 2007; Evonuk and Samuel, 2012).

In contrast to the $\mathrm{Ra}^* \sim 1$ zonal flow transition in Boussinesq spherical shells, there is not yet a consensus concerning the mechanisms that control the breakdown of the smaller-scale convection columns (e.g. Schmitz and Tilgner, 2009; King et al., 2012; King and Aurnou, 2012; Julien et al., 2012b,a). However, in low Ekman number Cartesian Boussinesq simulations, it is clear that the transition Ra^* values at which columnar modes become unstable is significantly less than unity. This low Ra^* breakdown criterion suggests that independent behavior transitions may exist for the large-scale zonal flows and the local-scale columnar convection modes.

In our simulations, however, the convection columns and the zonal flows seem to undergo simultaneous behavioral transitions. This may occur due to the moderate Ekman values at which we carry out our suite of simulations, or due to a difference in the stability properties of convection columns in spherical shell convection in the presence of zonal flows. Thus, we will focus here only on the one fundamental transition that separates the rapidly-rotating regime, in which columns exist and the equatorial zonal flow tends to be prograde (e.g. Gastine and Wicht, 2012), and the buoyancy-dominated regime, in which the columns are unstable and the equatorial zonal flows tend to be retrograde (e.g. Aurnou et al., 2007).

2.2. Numerical methods and boundary conditions

The numerical simulations of this parameter study have been carried out using the anelastic version of the code MagIC

(Wicht, 2002; Gastine and Wicht, 2012), which has been validated in the Jones et al. (2011) anelastic dynamo benchmark study. To solve the system of equations (3-6), $\tilde{\rho}\boldsymbol{u}$ is decomposed into a poloidal and a toroidal contribution

$$\tilde{\rho}\boldsymbol{u} = \nabla \times (\nabla \times W \boldsymbol{e_r}) + \nabla \times Z \boldsymbol{e_r}. \qquad (13)$$

W, Z, s and p are then expanded in spherical harmonic functions up to degree $\ell_{\max}$ in colatitude θ and longitude ϕ and in Chebyshev polynomials up to degree N_r in radius. A detailed description of the complete numerical method and the associated spectral transforms can be found in Gilman and Glatzmaier (1981). Typical numerical resolutions range from ($N_r = 65$, $\ell_{\max} = 85$) for Boussinesq models to ($N_r = 161$, $\ell_{\max} = 256$) for the most demanding anelastic models with $N_\rho = 5$. In the latter, a twofold or a fourfold symmetry in longitude has been used to ease numerical computation. As rapidly-rotating convection is dominated by high azimuthal wave numbers, this enforced symmetry is not considered to be influential on the averaged properties of the flow (e.g. Christensen, 2002; Heimpel et al., 2005; Jones and Kuzanyan, 2009). Note that this can influence the dynamics at high latitude where large-scale structures may evolve (e.g. polar vortices). However, this concerns only a very minor fraction of the total simulated volume.

In all the numerical models presented in this study, we have assumed constant entropy and stress-free mechanical boundary conditions at both spherical shell boundaries, r_i and r_o.

2.3. A parameter study

In this investigation, we consider two different Ekman numbers, E $= 10^{-3}$ and E $= 3 \times 10^{-4}$, which are rather moderate but allow us to carry out a significant number of strongly supercritical cases. Following our previous hydrodynamical models, the Prandtl number is set to 1 and we use a polytropic index $m = 2$ for the reference state. For all the models of this study, we employ an aspect ratio $\eta = 0.6$. This non-dimensional fluid layer depth exceeds those expected for the zonal flows in the gas giants (i.e. $0.85\,R_S$ and $0.96\,R_J$, see Liu et al., 2008; Heimpel and Gómez Pérez, 2011). However, this thicker shell geometry has the advantage of avoiding the significant numerical expense associated with spectral models of thin shell dynamics.

We have performed numerical simulations with various density contrasts spanning the range from $N_\rho = 10^{-2}$ (i.e. nearly Boussinesq) to $N_\rho = 5$ (i.e. $\rho_{\mathrm{bot}}/\rho_{\mathrm{top}} \simeq 150$). The strongest stratification considered here is still below the expected density contrast of the gas giants interiors: $N_\rho = 7.2$ between the 1 bar level and $0.96R_J$ (Nettelmann et al., 2012a; French et al., 2012) and $N_\rho = 7.7$ between the 1 bar level and $0.85R_S$ (Guillot, 1999). However, since the density gradient rapidly decreases with depth in both giant planets, a value of $N_\rho = 5$ covers more than 99% of the outward molecular envelope when starting at $0.96R_J$ (or $0.85R_S$). For each density stratification and Ekman number, we vary the Rayleigh number from onset of convection to $\mathcal{R}_m^* \sim 10$. Critical Rayleigh have been obtained with

Table 2: Critical Rayleigh numbers and corresponding azimuthal wave numbers for the different parameter regimes considered in this study.

Ekman number	N_ρ	Ra_c	m_{crit}
10^{-3}	0.01	1.412×10^4	10
10^{-3}	1	2.919×10^4	16
10^{-3}	3	8.126×10^4	29
10^{-3}	5	1.624×10^5	37
3×10^{-4}	0.01	5.075×10^4	15
3×10^{-4}	1	1.291×10^5	24
3×10^{-4}	3	3.714×10^5	47
3×10^{-4}	5	6.373×10^5	60

the linear stability code by Jones et al. (2009) and are given in Tab. 2.

Most of the runs have been initiated from a conductive thermal state (see Eq. 10) with a superimposed random entropy perturbation. For the most demanding high $\mathcal{R}_m^*$ cases, a converged solution at different parameter values has been used as a starting condition. Altogether, more than 125 simulations have been performed, each running for at least 0.3 viscous diffusion time such that a nonlinearly saturated state is reached (see Tab. A.4).

3. From rotation- to buoyancy-dominated regime

3.1. Convective flows

Figure 1 shows the radial velocity patterns when the supercriticality is gradually increased for two different density stratifications. In the rotation-dominated regime (i.e. $\mathcal{R}_m^* \ll 1$, upper panels of Fig. 1), the convective structures are aligned with the rotation axis following the Taylor-Proudman theorem. The azimuthal lengthscale of the convective columns is roughly three times smaller in the strongly stratified than in the Boussinesq model, following the critical wave numbers listed in Tab. 2. As shown in the linear stability analysis by Jones et al. (2009), this variation is due to the background density contrast that confines convection close to the outer boundary when N_ρ increases. This confinement causes the decrease in the typical length scales in both the radial and the azimuthal directions (see also Gastine and Wicht, 2012).

Convection develops both inside and outside the tangent cylinder in cases with more supercritical Rayleigh numbers that still have $\mathcal{R}_m^* \lesssim 1$ (Fig. 1, middle row). The integrity of the convective columns is disturbed due to the gradual loss of geostrophy as the buoyancy forcing increases in strength (e.g. Soderlund et al., 2012). The difference in lengthscales between the two cases is roughly retained at $r = 0.9\,r_o$. However, due to the local variations of the density scale height, the convective flow lengthscale increases in the deep interior of the $N_\rho = 5$ case (see for instance Fig. 5 in Gastine and Wicht, 2012).

The alignment of the convective features along the rotation axis is completely lost when buoyancy dominates the global-scale force balance ($\mathcal{R}_m^* \gtrsim 1$, lower panels of Fig. 1). While up- and downwellings have a very similar structure in the Boussinesq model, a strong asymmetry is visible in the strongly strat-
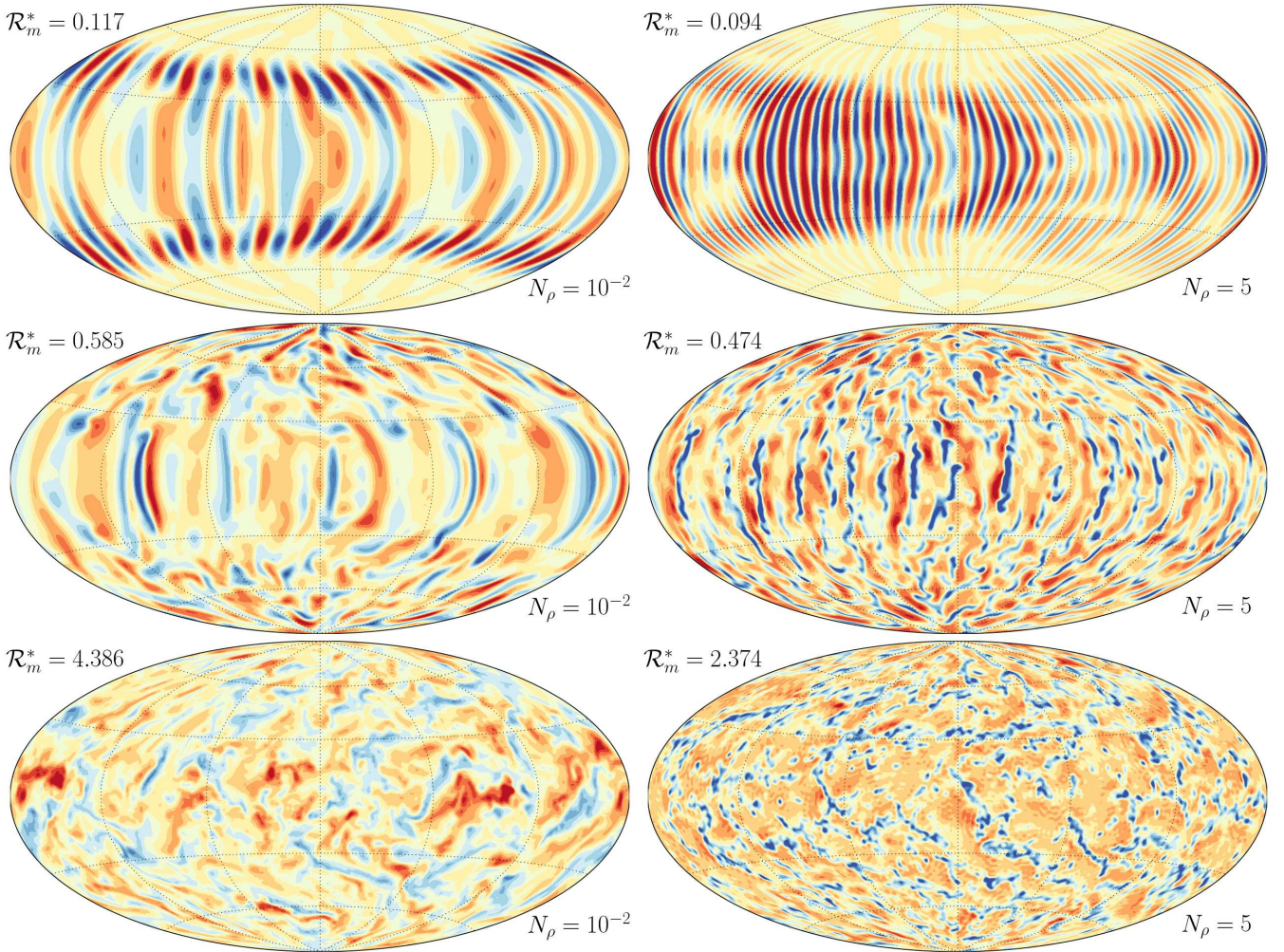
Figure 1: Radial velocity u_r at $r = 0.9\,r_o$ for six different numerical simulations with E = 10^{-3}. Boussinesq models (i.e. with $N_\rho = 10^{-2}$) with increasing $\mathcal{R}_m^*$ are displayed in the left panels, while anelastic models with $N_\rho = 5$ are displayed in the right panels. Outward flows are rendered in red, inward flows in blue.

ified case. Here the convection roughly forms a network of thin elongated downflows that enclose broader and weaker upflows. Upwelling structures tend to expand and acquire a mushroom-like shape, while downwelling plumes are narrow and concentrated. This network-like pattern of convection has been frequently observed in numerical models of the solar granulation (e.g. De Rosa et al., 2002; Miesch et al., 2008).

3.2. Zonal winds

Figure 2 shows the change in the zonal winds when $\mathcal{R}_m^*$ is increased in the nearly Boussinesq models ($N_\rho = 10^{-2}$, left panels) and in the strongly stratified models ($N_\rho = 5$, right panels). The typical pattern of an eastward (i.e., prograde) outer and a westward (i.e., prograde) inner geostrophic zonal flow already develops at mildly supercritical Rayleigh numbers (top row). These zonal flows are driven by Reynolds stresses (i.e. the statistical correlation of convective flow components), which rely on the prograde tilt of the convective columns induced by the boundary curvature (e.g. Busse, 1983; Zhang, 1992; Christensen, 2002). In the rotationally-dominated models, Reynolds stresses generate a positive angular momentum flux away from the rotation

axis that is balanced by viscous drag. Because of the strong confinement of convection close to the outer boundary in the $N_\rho = 5$ case, the equatorial jet is narrower than in the Boussinesq model. In addition, its amplitude is significantly larger than the amplitude of the adjacent retrograde jet in the stratified model.

With further increasing supercriticality, the differences discussed above tend to vanish. Thus, for $\mathcal{R}_m^* \lesssim 0.5 - 1$ (third panels), the equatorial jets have indeed very similar amplitudes and latitudinal extent while the retrograde jet is still somewhat weaker in the anelastic model. This agrees with the results or our previous parameter study in the $\mathcal{R}_m^* \lesssim 1$ regime (Gastine and Wicht, 2012). Note that the larger Ekman number cases considered here do not allow for the multiple jets solution found in Gastine and Wicht (2012), where the main equatorial jet was flanked by a retrograde zonal flow attached to the tangent cylinder and a pair of high latitude prograde jets.

When buoyancy starts to dominate the force balance (i.e. $\mathcal{R}_m^* \gtrsim 1$), the zonal flow direction largely reverses. The flow outside the tangent cylinder becomes mainly retrograde and the flow inside the tangent cylinder prograde. The amplitude of
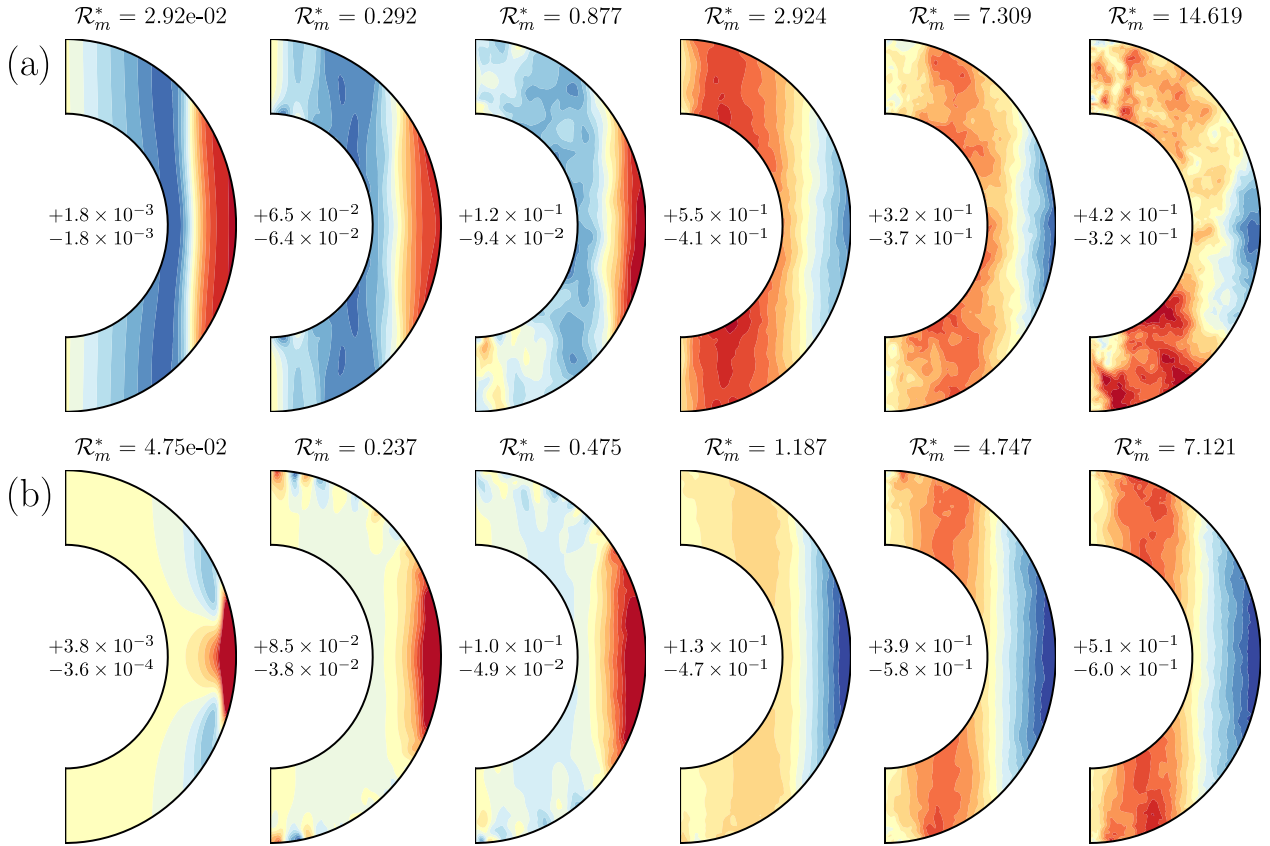
Figure 2: Zonally averaged azimuthal velocity in the meridian plane for simulations with E $= 10^{-3}$ and increasing $\mathcal{R}_m^*$. Upper panels correspond to Boussinesq models (i.e. $N_\rho = 10^{-2}$) and lower panels to $N_\rho = 5$. Colorscales are centered around zero: prograde jets are rendered in red, retrograde jets in blue. In some cases, the prograde contours have been truncated in amplitude to emphasise the structure of the retrograde flows. Extrema of the zonal flow velocity are indicated in the center of each panel (velocities are expressed in Rossby number units, i.e. $u/\Omega r_o$).

these zonal winds also increases roughly by a factor 5 at this transition reaching Ro $\simeq -0.5$. The zonal winds are nearly z-independent for $\mathcal{R}_m^* \simeq 1$ (fourth panels), even though the convective motions are no longer in geostrophic balance. However, a further increase of the supercriticality produces some pronounced smaller-scale z-dependent features in the Boussinesq models. These small-scale structures are highly time-dependent and would therefore cancel out when time-averaged quantities are considered. The last panels of Fig 2 show that both the mean zonal flow and the small-scale ageostrophic motions depend on the density contrast in the $\mathcal{R}_m^* \gg 1$ regime.

This change in the zonal flow structure is confirmed by the time-averaged toroidal kinetic energy spectra shown in Fig. 3 for four Boussinesq models at E $= 10^{-3}$. In the rotation-dominated regime ($\mathcal{R}_m^* < 1$, upper left panel), the spectrum peaks at $m = 0$, illustrating the strong contribution of axisymmetric zonal flows in the toroidal kinetic energy budget. For spherical harmonic orders $m > 20$, the spectra follow a clear power-law behaviour and the steep decrease (close to m^{-5}) is very similar to previous quasi-geostrophic studies computed at much lower Ekman numbers (E $= 10^{-8}$) (Schaeffer and Cardin, 2006) and matches the k^{-5} scaling derived by Rhines (1975) in the β-plane turbulence framework. Axisymmetric zonal flows still dominate the toroidal energy in the $\mathcal{R}_m^* = 2.92$ and
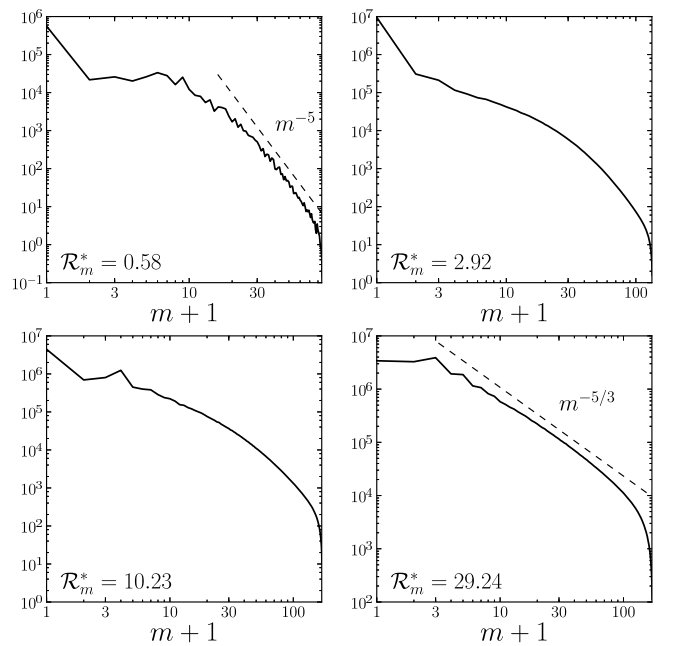

Figure 3: Time-averaged toroidal kinetic energy spectra for four different numerical models with $N_\rho = 10^{-2}$ and E $= 10^{-3}$.
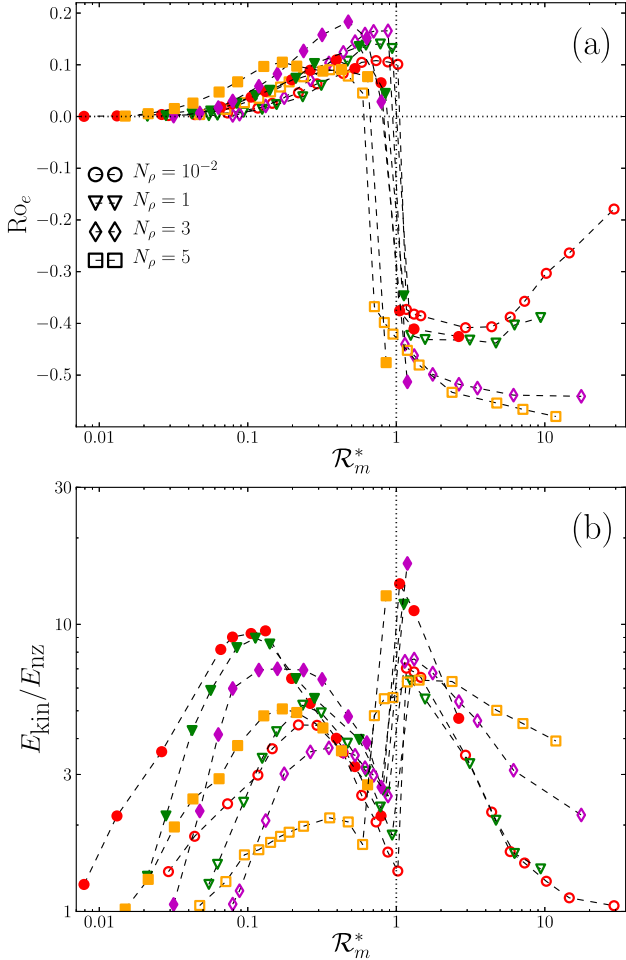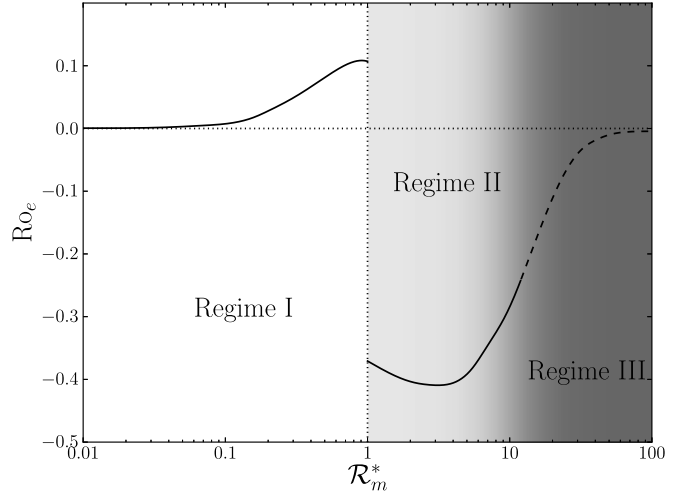
6

Figure 5: Regime diagram of the mean surface zonal flow at the equator as a function of $\mathcal{R}_m^*$. Regime I corresponds to the rotation-dominated regime, in which $\mathcal{R}_m^* \lesssim 1$. Regime II corresponds to the buoyancy-dominated regime in which the mixing of the angular momentum per unit of mass is efficient, while Regime III suggests a possible suppression of the zonal flow for $\mathcal{R}_m^* \gg 1$. This regime diagram is based on the Boussinesq cases from Fig. 4.

$$E_{\text{kin}} = \frac{1}{\tau} \frac{1}{V} \int_{t_0}^{t_0+\tau} \int_V \tilde{\rho} \boldsymbol{u}^2 \, dV \, dt, \qquad (14)$$

where V is the volume of the spherical shell and τ is the time-averaging interval. Each numerical simulation has been averaged long enough to suppress the short term variations.

Figure 4 shows how the surface equatorial zonal flow amplitude Ro_e and the ratio $E_{\text{kin}}/E_{\text{nz}}$ change when $\mathcal{R}_m^*$ is increased for numerical models with different Ekman numbers and density contrasts. In the rotation-dominated regime ($\mathcal{R}_m^* \lesssim 1$), the equatorial jets is always prograde and its amplitude gradually increases with $\mathcal{R}_m^*$. A maximum amplitude of $\text{Ro}_e \simeq 0.1 - 0.15$ is reached around $\mathcal{R}_m^* \simeq 0.5 - 0.8$. In this regime, the influence of the density contrast is not obvious: the $N_\rho = 3$ cases produce stronger jets than the Boussinesq models, which are, rather similar to the strongly stratified $N_\rho = 5$ cases.

Figure 4b shows that the ratio $E_{\text{kin}}/E_{\text{nz}}$ first increases for weak to moderate supercriticalities before decaying once convection is strongly driven. This decay is attributed to the gradual decorrelation of the convective flow components in the strongly-driven regime, which reduces the efficiency of the energy transfer between small-scale convection and large-scale mean zonal flows via Reynolds stresses (Christensen, 2002; Gastine and Wicht, 2012). The maximum of this ratio depends on both the density stratification and the Ekman number. In Boussinesq models at $E = 3 \times 10^{-4}$, this maximum is around 10 (which means to 90% of the total kinetic energy is contained in the zonal flows) while it reaches only 5 (i.e. 80%) in the $N_\rho = 5$ models. In addition, decreasing the Ekman number tends to produce a stronger zonal flow contribution (see Christensen, 2002).

An abrupt transition to retrograde equatorial zonal winds takes place close to $\mathcal{R}_m^* \simeq 1$, independently of the density strat-

Figure 4: (a) Amplitude of the surface zonal wind at the equator (in units of $\text{Ro}_e = u_\phi/\Omega r_o$) plotted against $\mathcal{R}_m^*$. (b) Ratio of total over non-zonal kinetic energy plotted against $\mathcal{R}_m^*$. In both panels, closed symbols correspond to simulations with $E = 3 \times 10^{-4}$ and open symbols to simulations with $E = 10^{-3}$. The transition at $\mathcal{R}_m^* = 1$ is emphasised by a dotted vertical line.

$\mathcal{R}_m^* = 10.23$ cases, but the slope at smaller lengthscales flattens gradually. At $\mathcal{R}_m^* = 29.24$ (lower right panel), the spectrum shows a mild maximum at $m = 2$ before clearly following an inertial range scaling of $m^{-5/3}$, the theoretical behaviour expected for homogeneous and isotropic 3-D turbulence (e.g. Lesieur, 1997). In this case, the axisymmetric zonal flow contribution is not dominant anymore as already suggested by the last panel of Fig. 2a.

3.3. Convection regimes

To further investigate the change in zonal flow regime observed in Figs. 1-2, we consider time-averaged quantities for the whole set of numerical models computed in this parameter study. We focus in the following on the zonal flow amplitude characterised by the dimensionless Rossby number $\text{Ro} = \overline{u}_\phi/\Omega r_o$ and on the contribution of axisymmetric toroidal energy in the total kinetic energy budget. Following Christensen (2002), this is quantified by the ratio of the total to the non-zonal kinetic energy $E_{\text{kin}}/E_{\text{nz}}$, where E_{kin} has been obtained by

ification and the Ekman number considered. The retrograde equatorial jet amplitude is roughly multiplied by a factor 4 at this transition to reach $\mathrm{Ro}_e \simeq -0.4$. This goes along with a larger $E_{\mathrm{kin}}/E_{\mathrm{nz}}$ value that reaches approximately 7 for the $E = 10^{-3}$ cases (i.e. 85%) and 15 for the $E = 3 \times 10^{-4}$ cases (i.e. 93%).

As $\mathcal{R}_m^*$ is increased further, the density stratification starts to play a more important role. For stronger stratifications, the equatorial zonal flow amplitude further increases while it roughly levels off and finally decreases in the Boussinesq models. This is also reflected in the variation of $E_{\mathrm{kin}}/E_{\mathrm{nz}}$ where the strongly stratified cases decay slower at large $\mathcal{R}_m^*$ than the weakly stratified models. Since we expect that the convective fluctuations will dominate the mean zonal flows at $\mathcal{R}_m^* \gg 1$, the ratio $E_{\mathrm{kin}} \simeq E_{\mathrm{nz}}$ should ultimately tend to unity. This is already observed in Boussinesq cases in Fig. 4b where a value of 1.04 is reached at $\mathcal{R}_m^* = 29.24$. For the stronger stratified cases, much larger $\mathcal{R}_m^*$ values are required than we could afford to simulate numerically.

Figure 5 shows a tentative regime diagram based on our simulation results. Regime I corresponds to rotation-dominated cases ($\mathcal{R}_m^* < 1$) where convection shows a columnar structure and maintains a prograde equatorial zonal flow. Regime II is characterised by three-dimensional convection and a strong retrograde equatorial jet. The transition between regimes I and II takes place around $\mathcal{R}_m^* \sim 1$ independently of the density stratification and the Ekman number. The strong decrease of the zonal flow amplitude observed in the Boussinesq models for $\mathcal{R}_m^* > 5$ points toward a possible third regime in which the zonal flows are insignificant and convection becomes isotropic. The transition between regimes II and III is however gradual and rather difficult to pinpoint (emphasised by the dashed-line and the color gradient in Fig. 5). Our simulations suggest for instance that the transition depends on the density stratification.

The reason for the density-dependent jets amplitude observed in the buoyancy-dominated regime and the possibility of a third regime at large Ra^* are further discussed in the next section.

4. Angular momentum mixing

4.1. Influence of the density stratification

When buoyancy dominates Coriolis force, strong convection can locally mix the angular momentum. Flows in which angular momentum is indeed homogenised have been found in several studies of atmospheric dynamics or numerical models of rotating convection with a weak rotational influence (e.g. Gilman, 1977; Hathaway, 1982; De Rosa et al., 2002; Aurnou et al., 2007; Bessolaz and Brun, 2011).

In an inertial reference frame, the angular momentum of a fluid parcel is given by

$$\mathcal{M} = \mathcal{M}_{\mathrm{ZF}} + \mathcal{M}_{\mathrm{PR}} = \rho \overline{u}_\phi s \, \delta\mathcal{V} + \rho \Omega s^2 \, \delta\mathcal{V}, \qquad (15)$$

where $\delta\mathcal{V}$ is the volume of the fluid element, $s = r \sin\theta$ is the cylindrical radius, $\mathcal{M}_{\mathrm{ZF}}$ is the angular momentum due to zonal flows and $\mathcal{M}_{\mathrm{PR}}$ is the angular momentum that comes from the planetary rotation. The overbars here indicate an azimuthal
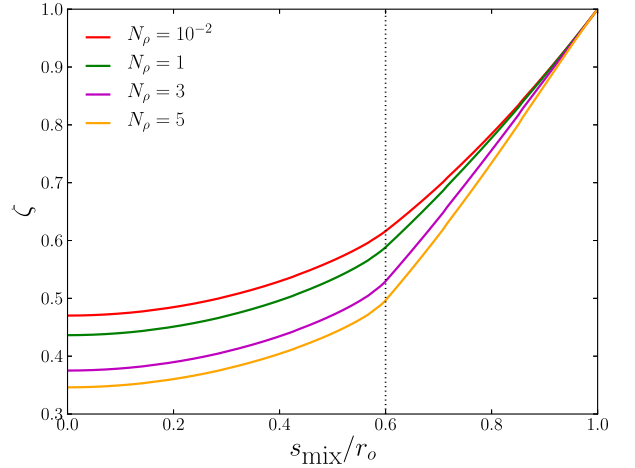

Figure 6: Profiles of ζ for different density stratifications as a function of s_{mix}, the minimum cylindrical radius above which mixing of angular momentum per unit of mass occurs. The vertical line corresponds to the location of the tangent cylinder.

Table 3: ζ from Eq. (18) and ζ_{TC} for different density stratifications.

N_ρ	ζ	ζ_{TC}
0.01	0.470	0.616
1	0.436	0.588
3	0.375	0.529
5	0.346	0.496

average. Because of the anelastic continuity equation (3), the mass of a fluid element is conserved during its displacement such that $\rho\delta\mathcal{V} = $ const.. If, in addition, a fluid parcel conserves its angular momentum $\mathcal{M}$, then, as hypothesized by Gilman and Foukal (1979), the angular momentum *per unit of mass* $\mathcal{L}$ is a conserved quantity

$$\mathcal{L} = \mathcal{L}_{\mathrm{ZF}} + \mathcal{L}_{\mathrm{PR}} = \overline{u}_\phi s + \Omega s^2 = \text{const.} \qquad (16)$$

Nondimensionalising this equation by Ωr_o^2 leads to

$$\mathcal{L}^* = \mathrm{Ro}\frac{s}{r_o} + \frac{s^2}{r_o^2}. \qquad (17)$$

A spatially homogeneous $\mathcal{L}^*$ value would then equal the mass integral of the initial angular momentum distribution (i.e. a rigid body rotation) given by

$$
\begin{aligned}
\zeta = \langle \mathcal{L}^* \rangle_\rho &= \frac{1}{m} \int_V \mathcal{L}_{\mathrm{PR}}^* dm \\
&= \frac{1}{m} \int_0^{2\pi} \int_0^\pi \int_{r_i}^{r_o} \left[\frac{\tilde{\rho}(r)s^2}{r_o^2} \right] r^2 \sin\theta \, dr \, d\theta \, d\phi,
\end{aligned}
\qquad (18)
$$

where m is the total mass of the spherical shell given by $m = \int_V \tilde{\rho}(r)dV$. ζ depends on the background density stratification and decreases by 25% when the density contrast is increased from nearly Boussinesq ($N_\rho = 10^{-2}$) to $N_\rho = 5$ cases (see the middle column of Tab. 3). This decrease of ζ explains the differences in equatorial jet amplitudes in Fig. 4 via
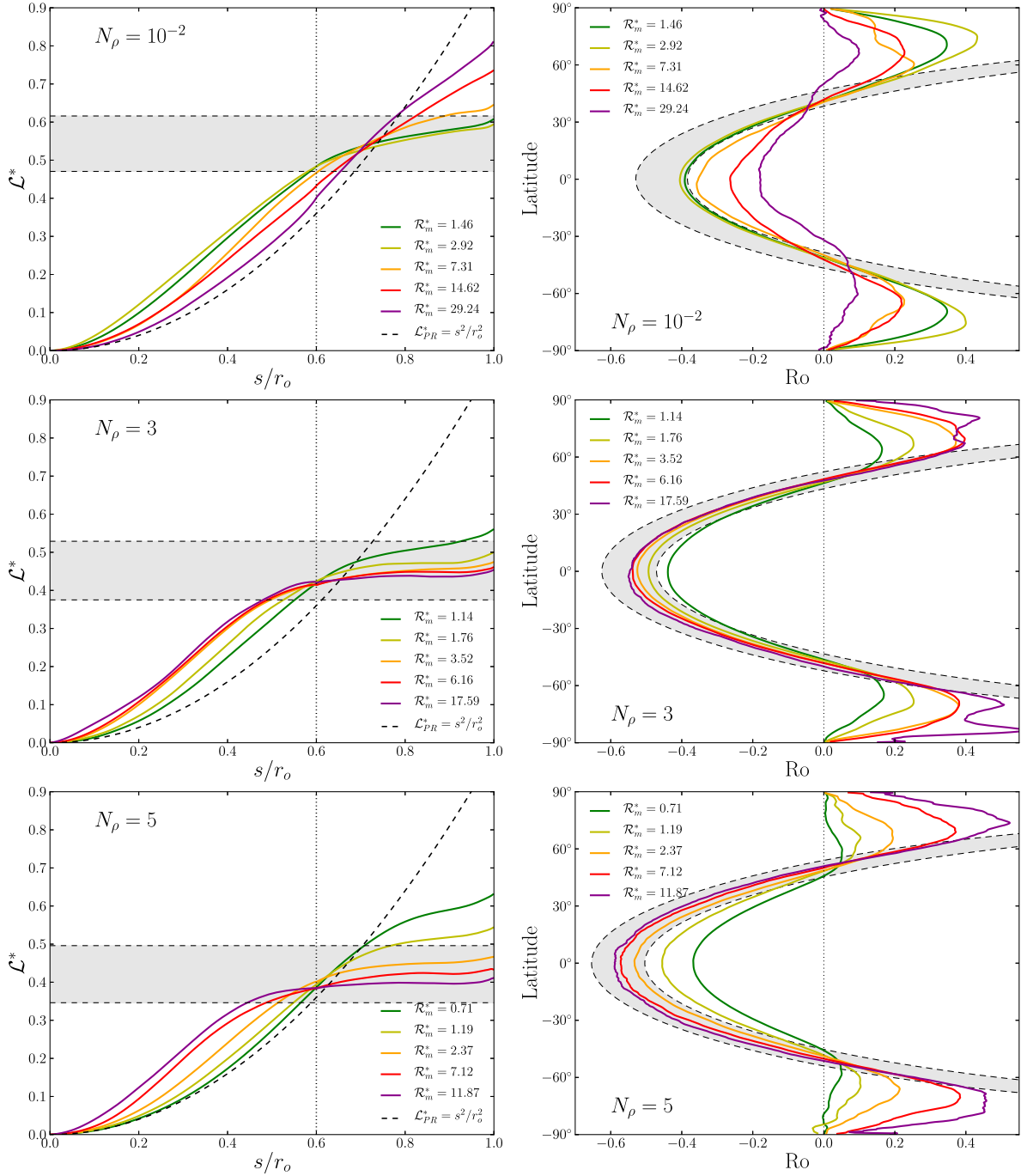
Figure 7: Left: time-averaged specific angular momentum plotted against the cylindrical radius s for various numerical simulations with $E = 10^{-3}$. Right: corresponding azimuthally-averaged velocity profiles as a function of latitude at the outer boundary. The vertical lines in the left panels correspond to the tangent cylinder. For comparison, the grey-shaded area are delimited by the theoretical values associated with $\mathcal{L}^*$ mixing over the whole spherical shell (lower bound) and outside the tangent cylinder only (upper bound, see Tab. 3 for the corresponding values).

$$\text{Ro} = \zeta \frac{r_o}{s} - \frac{s}{r_o}. \qquad (19)$$

Note that Aurnou et al. (2007) derived the Boussinesq version of Eq. (19), in which the background density is homogeneous.

4.2. Partial mixing of $\mathcal{L}^*$

The previous derivation provides an idealised description of the simulation results at $\mathcal{R}_m^* \gg 1$. For instance, the equatorial zonal flows, shown in Fig. 4, never reach the maximum theoretical amplitudes of $\text{Ro}_e = -0.528$ for $N_\rho = 10^{-2}$ and $\text{Ro}_e = -0.654$ for $N_\rho = 5$ predicted by Eq. (19). From this we suspect that the mixing of $\mathcal{L}^*$ takes place in only part of the spherical shell.

9
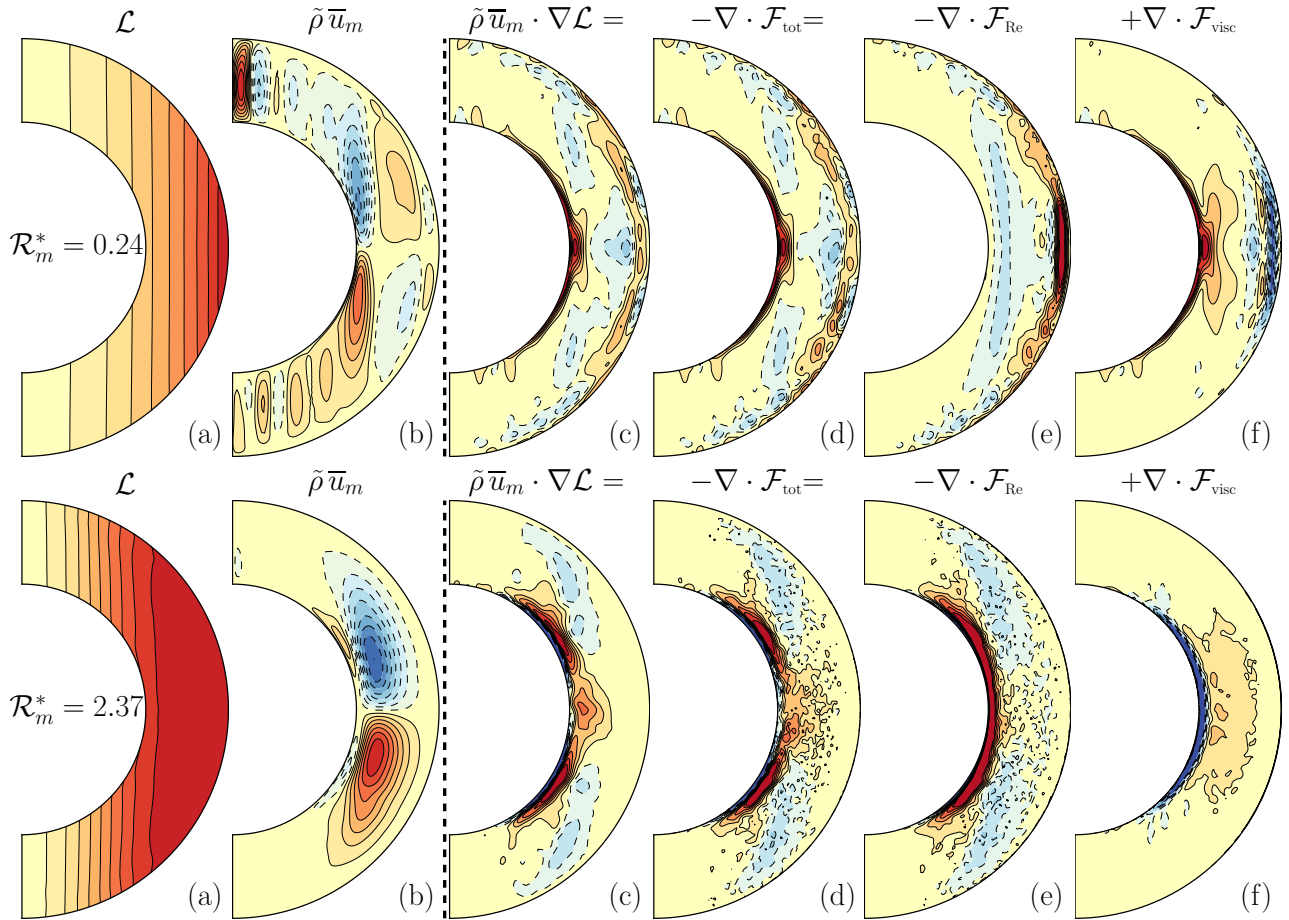
Figure 8: Azimuthal force balance for two numerical models with $\mathcal{R}_m^* = 0.24$ (upper panels) and $\mathcal{R}_m^* = 2.37$ (lower panels). Both cases have $N_\rho = 5$ and E $= 10^{-3}$. (a) Time-averaged angular momentum per unit of mass $\mathcal{L}^*$. (b) Time-averaged stream-function of the meridional circulation $\tilde{\rho}\,\overline{u}_m$. (c) Advection of the angular momentum $\mathcal{L}^*$ by the mean meridional circulation, i.e. left-hand side of Eq. (21). (d) The net axial torque of the right-hand side of Eq. (21). (e) The contribution of Reynolds stresses to this torque. (f) The contribution of viscous stresses to this axial torque. For each panel, positive (negative) values are rendered in red (blue). Panels (d-f) share the same contour levels.

We can then make the following *ad-hoc* assumption that $\mathcal{L}^*$ is homogenised for cylindrical radii $s > s_{\text{mix}}$ only. This leads to

$$\zeta_{s_{\text{mix}}} = \frac{1}{m(s_{\text{mix}})} \int_{z(s)} \int_0^{2\pi} \int_{s_{\text{mix}}}^{r_o} \left[\frac{\tilde{\rho}(r)s^2}{r_o^2} \right] s\, ds\, d\phi\, dz, \qquad (20)$$

where $z(s) = \pm\sqrt{r_o^2 - s^2}$ outside the tangent cylinder and $\pm\left(\sqrt{r_o^2 - s^2} - \sqrt{r_i^2 - s^2}\right)$ inside. Figure 6 shows the variation of $\zeta_{s_{\text{mix}}}$ for different density stratifications as a function of s_{mix}. When the shell is only partially mixed the influence of the density stratification is gradually reduced and becomes negligible when $\mathcal{L}^*$ is homogenised in only a small fraction of the domain. Because the tangent cylinder is often considered to present a dynamical barrier for rotation-dominated convection, Aurnou et al. (2007) introduced the respective values for mixing outside the tangent cylinder only. Note, however, that this is a rather arbitrary choice since there is no expected sharp vorticity step across the tangent cylinder in the regime II discussed here. The third column in Tab. 3 corresponds to these cases (also see the dotted lines in Fig. 6). In the Boussinesq limit we

recover $\zeta_{TC} = 1 - \frac{3}{5}(1 - \eta^2)$ already derived by Aurnou et al. (2007).

Figure 7 displays time-averaged cylindrically radial profiles of $\mathcal{L}^*$ and latitudinal profiles of surface zonal flows for numerical simulations in the buoyancy-dominated regime (Regime II). For each panel, the grey-shaded area shows the spans between the theoretical $\mathcal{L}^*$-mixing over the entire shell and outside the tangent cylinder only. For comparison, a solid body rotation profile is demarcated by the dashed black lines in the left panels of Fig. 7.

For $\mathcal{R}_m^* \simeq 1$ (dark green lines), the $\mathcal{L}^*$ profiles are roughly constant outside the tangent cylinder in the Boussinesq models. From Tab. 3 and Fig. 6, we therefore predict a value of $\text{Ro}_e = \zeta_{s_{\text{mix}}} - 1 \simeq -0.4$ consistent with the numerical surface value of $\text{Ro}_e = -0.385$ (see Tab. A.4). In contrast, $\mathcal{L}^*$-mixing occurs only in a relatively thin region ($s > 0.7 - 0.8\, r_o$) in the $N_\rho = 5$ case. Predictions for Ro_e for this range of mixing depths lie between -0.25 and -0.4, consistent with the numerical value of $\text{Ro}_e = -0.368$.

In the strongly stratified cases ($N_\rho \geq 3$), the $\mathcal{L}^*$-mixing moves deeper when $\mathcal{R}_m^*$ is increased. The entire region outside

the tangent cylinder is homogenized (light green line for $N_\rho = 3$ and orange line for $N_\rho = 5$) and the surface zonal flows match the theoretical profile derived before, at least at mid latitudes (i.e. $\theta \lesssim \pm 50°$) once $\mathcal{R}_m^* \simeq 2$. For $\mathcal{R}_m^* > 10$, $\mathcal{L}^*$ is constant for $s > 0.5\, r_o$ and the zonal flow profiles lie roughly midway between the two theoretical curves (fully-mixed and $s_{\mathrm{mix}} = \overline{s_{TC}}$ limits). They reach stronger amplitude in the $N_\rho = 5$ cases due to the larger available $\mathcal{L}^*$ reservoir (Fig. 6).

The profiles also show that the $\mathcal{L}^*$-mixing stops in the highest $\mathcal{R}_m^*$ Boussinesq models (dark purple line) and gradually tends toward the solid body rotation , i.e. $\mathcal{L}^* = s^2/r_o^2$. As described before, this weakening of the zonal flow at the highest accessible values of $\mathcal{R}_m^*$ appears to define a third dynamical regime.

4.3. Azimuthal force balance and meridional flow structure

In this section, we explore how the zonal flows are maintained in the $\mathcal{L}^*$-mixing regime (Regime II in Fig. 5) and the possible decay of these flows at larger $\mathcal{R}_m^*$ (Regime III). To do so, we analyse the axisymmetric, azimuthal component of the Navier-Stokes equations (Eq. 4) following Miesch and Hindman (2011) and Brun et al. (2011):

$$
\begin{aligned}
\tilde{\rho}\frac{\partial \overline{u}_\phi}{\partial t} + \tilde{\rho}\,\overline{\boldsymbol{u}}_m \cdot \boldsymbol{\nabla}\mathcal{L} &= -\boldsymbol{\nabla}\cdot\mathcal{F}_{\mathrm{tot}}, \\
&= -\boldsymbol{\nabla}\cdot[\mathcal{F}_{\mathrm{Re}} - \mathcal{F}_{\mathrm{visc}}], \qquad (21)\\
&= -\boldsymbol{\nabla}\cdot\left[\tilde{\rho}\, s\, \overline{\boldsymbol{u}'u'_\phi} - \mathrm{E}\,\tilde{\rho}\, s^2\, \boldsymbol{\nabla}\!\left(\frac{\overline{u}_\phi}{s}\right)\right],
\end{aligned}
$$

where $\overline{\boldsymbol{u}}_m$ is the mean meridional circulation, $\mathcal{L} = s\overline{u}_\phi + s^2$ is the angular momentum per unit of mass, $\mathcal{F}_{\mathrm{tot}}$ is the angular momentum flux associated with Reynolds and viscous stresses, $\mathcal{F}_{\mathrm{Re}}$ and $\mathcal{F}_{\mathrm{visc}}$, respectively. Primed quantities correspond to fluctuations about the axisymmetric mean. Equation (21) requires that the advection of axisymmetric angular momentum by the meridional flow is balanced, on time-average, by the net axial torques due to Reynolds stresses and viscosity.

Figure 8 shows the angular momentum per unit of mass and the mean meridional flow, along with the different contributions of this force balance for two strongly stratified numerical models with $\mathcal{R}_m^* = 0.24$ and $\mathcal{R}_m^* = 2.37$. In the rotation-dominated case ($\mathcal{R}_m^* = 2.37$, upper panels), the equatorial zonal wind is prograde and $\mathcal{L}$ gradually increases with cylindrical radius s. In the buoyancy-dominated case ($\mathcal{R}_m^* = 2.37$, lower panels), $\mathcal{L}$ is roughly constant outside the tangent cylinder (see also the orange curve in the last row of Fig. 7) and is associated with a strong retrograde equatorial jet which reaches $\mathrm{Ro}_e \simeq -0.5$.

The meridional circulation patterns differ between the two numerical models shown in Figure 8. While a relatively small-scale multicellular meridional circulation structure is observed in the first case, the meridional flow in the second model is dominated by a pair of large-scale cells. In the latter, a second pair of weaker counter-cells is discernable close to the inner boundary. Such a transition between small-scale multicellular and large-scale single-celled meridional circulation has been already observed for numerical simulations around $\mathcal{R}_m^* \sim 1$ (e.g. Elliott et al., 2000; Bessolaz and Brun, 2011).
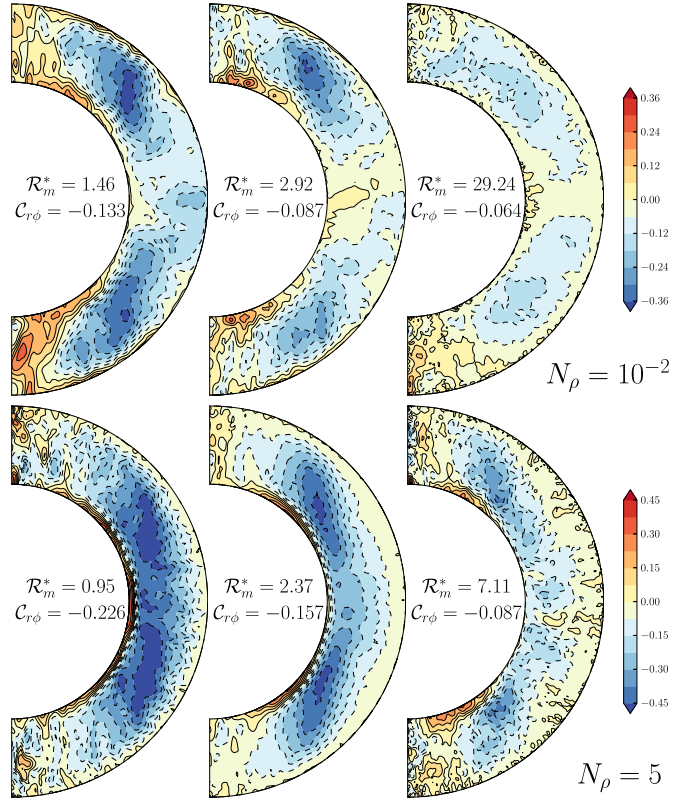
Figure 9: Correlation $C_{r\phi}$ for different numerical models in regime II with $N_\rho = 10^{-2}$, E $= 10^{-3}$ (upper panels) and $N_\rho = 5$, E $= 10^{-3}$ (lower panels). The average correlation $C_{r\phi}$ throughout the shell is indicated in the middle of each panel.

This change of the meridional circulation pattern observed around $\mathcal{R}_m^* \simeq 1$ is reflected in the spatial variations of the force balance expressed by Eq. (21). The third and fourth panels of Fig. 8 check this balance and confirm that the advection of $\mathcal{L}$ by the mean meridional flow is indeed balanced, on time average, by the sum of the torques due to viscous and Reynolds stresses. Some small-scale time-dependent features remain visible in the $\mathcal{R}_m^* = 2.37$ case but will vanish if a longer averaging time is considered. In the $\mathcal{R}_m^* = 0.24$ case, viscous stresses (panel f) are significant and largely, but not perfectly, compensate the Reynolds stresses (panel e). This results in several sign changes in the axial torque (panel d) that are mirrored by the complex meridional flow structure (see also Augustson et al., 2012). This force balance is somewhat different in the $\mathcal{R}_m^* = 2.37$ model in which the simple large-scale Reynolds stresses dominate the force balance and drive the dominant pair of meridional circulation cells. The viscous contribution becomes significant only near the inner boundary and results in the second weaker pair of cells visible in Fig. 8b. The presence of these weak counter cells might however be sensitive to the type of mechanical and thermal boundary conditions employed in our models (see also Miesch et al., 2008).

4.4. Towards a possible third regime for $\mathcal{R}_m^* \gg 1$

Figure 8 shows that the Reynolds stresses become the dominant contribution to the net axial torque when $\mathcal{R}_m^* \gtrsim 1$. The

Figure 10: Time-averaged kinetic energy budget for the numerical simulations displayed in Fig. 7. Dark-grey area correspond to the non-zonal kinetic energy, black area to the kinetic energy contained in the axisymmetric poloidal flows (i.e. meridional circulation), and hatched light grey area to the energy in axisymmetric toroidal flow.

force balance (21) can thus be approximated in the $\mathcal{R}_m^* \gg 1$ regime by

$$\tilde{\rho}\,\overline{u}_m \cdot \boldsymbol{\nabla}\mathcal{L} \simeq -\boldsymbol{\nabla} \cdot \mathcal{F}_{\mathrm{Re}} \simeq -\boldsymbol{\nabla} \cdot \left[\tilde{\rho} s\,\overline{\boldsymbol{u'}\boldsymbol{u'_\phi}}\right], \qquad (22)$$
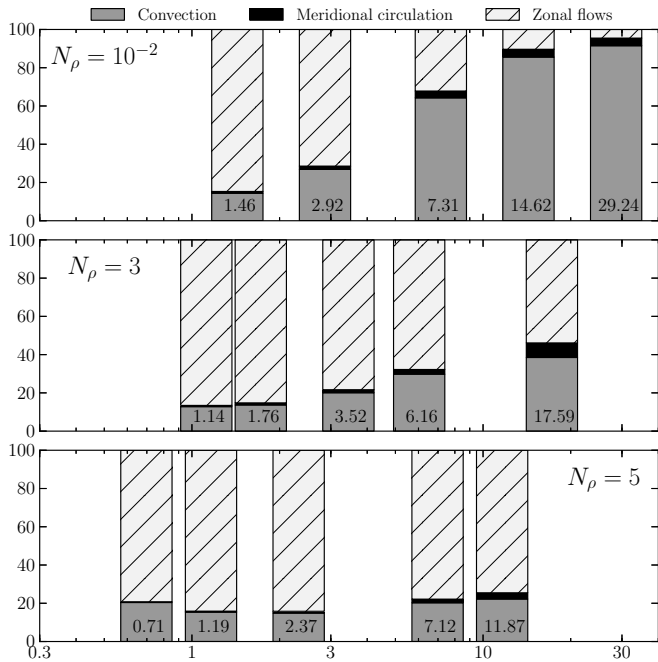
since viscosity does not play a significant role here. This balance shows that Reynolds stresses rely on the correlations between the meridional and the longitudinal components of the convective flow $\overline{u'_r u'_\phi}$ and $\overline{u'_\theta u'_\phi}$ (e.g. Ruediger, 1989; Käpylä et al., 2011b). In the following, we focus on the change in $\overline{u'_r u'_\phi}$ only and quantify the correlation by

$$C_{r\phi} = \frac{\overline{u'_r u'_\phi}}{\left(\overline{u'^2_r}\,\overline{u'^2_\phi}\right)^{1/2}}, \qquad (23)$$

where the overbars correspond to an azimuthal average. Figure 9 shows the variation of $C_{r\phi}$ when $\mathcal{R}_m^*$ is increased in Boussinesq (upper panels) and in strongly stratified models (lower panels). For $\mathcal{R}_m^* \simeq 1$, the correlations are significant and strong negative Reynolds stresses are maintained. However, $C_{r\phi}$ gradually decreases in the more supercritical cases. An increase of the Rayleigh number indeed goes along with stronger turbulent velocities and smaller typical flow lengthscales, leading to a gradual decrease of the turnover timescale of convection. Small-scale eddies are not influenced by rotation anymore since their lifetime becomes significantly smaller than the rotation period (see also Gastine and Wicht, 2012, for the rotation-dominated cases). This loss of coherence results in a gradual decrease of the Reynolds stresses correlations needed to maintain the mean flows (Brummell et al., 1998; Miesch et al., 2000;

Käpylä et al., 2011b). A reduction of the mean flows amplitude is therefore anticipated when the motions become more turbulent.

Figure 10 shows the energy distribution for numerical models in the buoyancy-dominated regime (see Fig. 7 for the corresponding zonal flows). Zonal flows dominate the energy budget for $\mathcal{R}_m^* \simeq 1$ (80-90%). In Boussinesq models, the contribution of the turbulent flows then increases rapidly to overwhelm the energy distribution for $\mathcal{R}_m^* > 10$. This increase is more gradual for the $N_\rho = 3$ cases and it even seems to level around 20% in the $N_\rho = 5$ models. This reflects the density-dependent evolution of $E_{\mathrm{kin}}/E_{\mathrm{nz}}$ in the $\mathcal{R}_m^* \gg 1$ regime visible in Fig. 4b.

This decorrelation defines a gradual transition towards the possible regime III displayed in Fig. 5. When the degree of turbulence increases and the small-scale motions dominate the energy budget, a decrease of zonal flows amplitudes is observed in Boussinesq and $N_\rho = 1$ models due to the gradual loss of correlation of the convective flow. However, this scenario still needs to be confirmed in strongly stratified models: the presently accessible range of $\mathcal{R}_m^*$ allows for only weakly turbulent convective motions in our $N_\rho \geq 3$ simulations (see Tab. A.4).

5. A transitional regime in anelastic models

As mentioned in section 2, $\mathcal{R}^*$ is a radially-dependent quantity that can vary across the fluid shell by several orders of magnitude in the strongly stratified models. This can lead to different dynamical regimes close to the outer boundary and in the fluid shell's deeper interior.

5.1. Convective flows in the transitional regime

Figure 11 shows the variation of $\mathcal{R}^*(r)$ for different numerical models with $N_\rho = 5$. The spherical shell can be separated in two distinct layers: $\mathcal{R}^* > 1$ close to the outer boundary where buoyancy effects become large and $\mathcal{R}^* < 1$ in the deep interior where rotation can still dominate the force balance. As $\mathcal{R}_m^*$ increases, the buoyancy-dominated region grows inward. The radius r_{mix} is defined by the radius at which $\mathcal{R}^* = 1$ approximately separating the buoyancy-dominated region from the rotation-dominated inner region. Figure 12 sketchs this *transitional regime* in which columnar convection in the deep interior exists contemporaneously with three-dimensional convective structures close to the outer boundary.

Figure 13, showing equatorial cuts of ω_z for numerical models with $N_\rho = 5$ and three different Rayleigh numbers, confirms that r_{mix} indeed coincides with a dynamical regime boundary. In the inner part, the convective flow is dominated by convective columns tilted in the prograde direction (positive vorticity dominates) that maintain Reynolds stresses. Beyond r_{mix}, the convective flow seems to be more radially-oriented with no preferred sign of vorticity anymore. Some strongly-stratified simulations discussed in our previous study already show the very beginning of this transitional regime (see Fig. 14 in Gastine and Wicht, 2012).
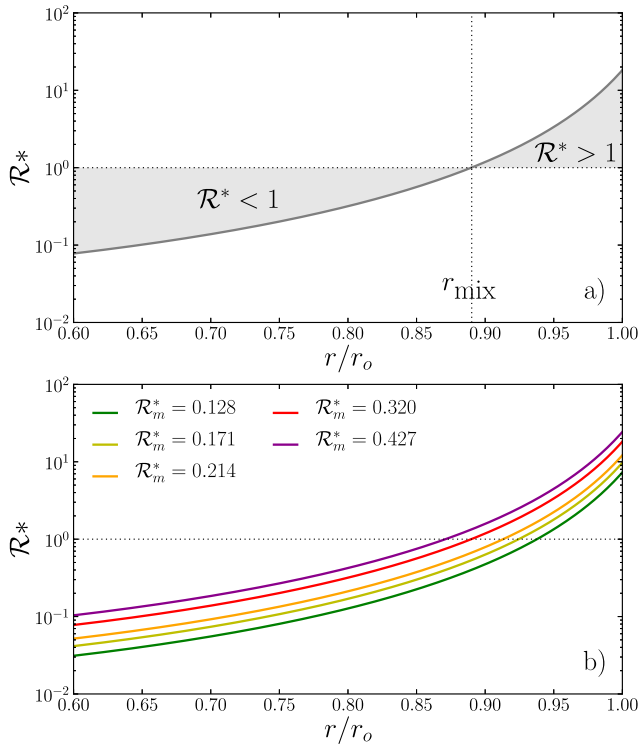
Figure 11: (a) Sketch of the radial profile of $\mathcal{R}^*$ in strongly stratified models. r_{mix} corresponds to the radius at which $\mathcal{R}^* = 1$. It marks the tentative limit between the buoyancy-dominated region ($\mathcal{R}^* > 1$) and the rotation-dominated region ($\mathcal{R}^* < 1$), both emphasised by a grey-shaded area. (b) Radial profile of $\mathcal{R}^*$ for various numerical simulations with $N_\rho = 5$ and $E = 3 \times 10^{-4}$.

5.2. Zonal flows in the transitional regime

The transition to regime II happens when r_{mix} reaches approximately mid-depth, where an abrupt transition to a retrograde equatorial jet takes place. The parameter space, where the transitional regime with two distinct types of convection coexists, is therefore quite narrow. Strong stratification is required and $\mathcal{R}_m^*$ has to be neither too small nor too large, typically in the $\mathcal{R}_m^* \simeq 0.1 - 0.5$ range.

Figure 14 shows the surface zonal flows for numerical models that lie in this specific range of parameters. Typical for numerical simulations at moderate Ekman numbers (here $E = 3 \times 10^{-4}$) that are still in the $\mathcal{R}_m^* < 1$ regime, a large prograde equatorial jet is flanked by two weaker retrograde jets at higher latitudes ($\pm 60°$). Due to the aspect ratio of the spherical shell considered in this study ($\eta = 0.6$), the prograde equatorial wind extends up to mid latitudes of $\pm 50°$. For $\mathcal{R}_m^* = 0.128$ (green line), the zonal wind maximum is reached at the equator, similarly to Boussinesq models (e.g. Heimpel et al., 2005). However, when increasing $\mathcal{R}_m^*$, the center of the main equatorial jet decreases until eventually a dimple appears flanked by two maxima. The width of the dimple further grows with $\mathcal{R}_m^*$ while the central flow amplitude decreases reaching approximately $\pm 25°$ latitude and 20% of the maximum zonal wind amplitude just before the transition to regime II (see the inset in Fig. 14). Such a pronounced dimple has also been observed in the anelastic models by Kaspi et al. (2009) who also employed
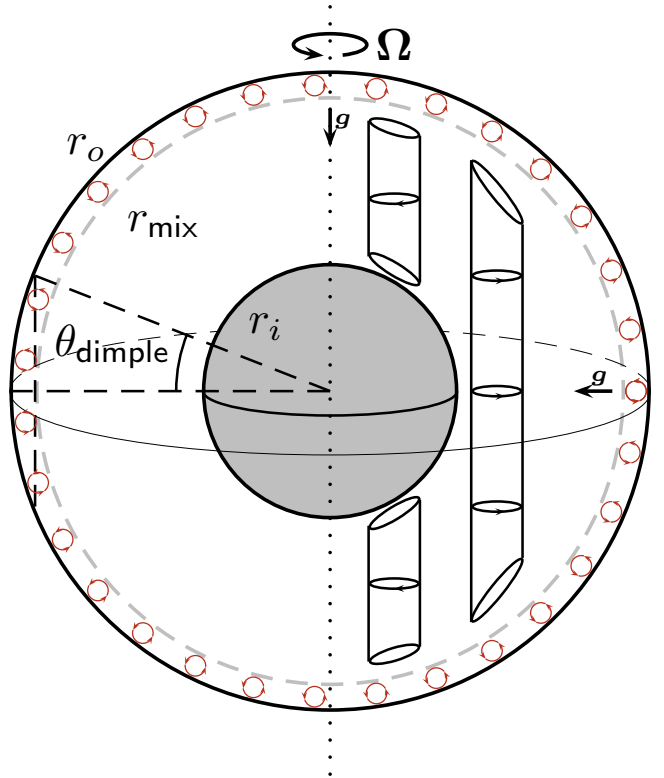
Figure 12: Sketch illustrating the transitional regime in strongly stratified models.

strong density contrasts (see Fig. 13 in their study).

Following the sketch displayed in Fig. 12, this dimple can be directly related to the transition between rotation-dominated and buoyancy-dominated regions. As already shown in Fig. 13, r_{mix} separates these two regions and thus allows us to roughly estimate the typical latitudinal extent of the dimple via a simple geometrical relation (see Fig. 12)

$$\cos\theta_{\mathrm{dimple}} \sim \frac{r_{\mathrm{mix}}}{r_o}. \qquad (24)$$

This simple expression thus relates the latitudinal extent of the observed surface zonal flows to the transition radius between the two distinct internal dynamical regimes. Although this expression is rather crude in predicting the exact width of the dimple (see the two magenta lines in Fig. 14), it can be used as an order of magnitude estimate of its latitudinal extent.

5.3. A dimple in the equatorial zonal band of Jupiter

A similar dimple exists on Jupiter (Fig. 15) and extends roughly between $\pm 7°$ latitude. The amplitude of the equatorial wind decreases by roughly 30% at the equator. Is Jupiter's dimple the surface expression of an internal regime transition? From Eq. (24) with $\theta_{\mathrm{dimple}} \sim 7°$, we can speculate that the mixing radius r_{mix} would lie around 500 km below the 1 bar level.

To evaluate the plausibility of this scenario, we try to establish the value $\mathcal{R}_{\mathrm{surf}}^*$ of Jupiter using the scaling laws by Christensen (2002); Christensen and Aubert (2006) and

13
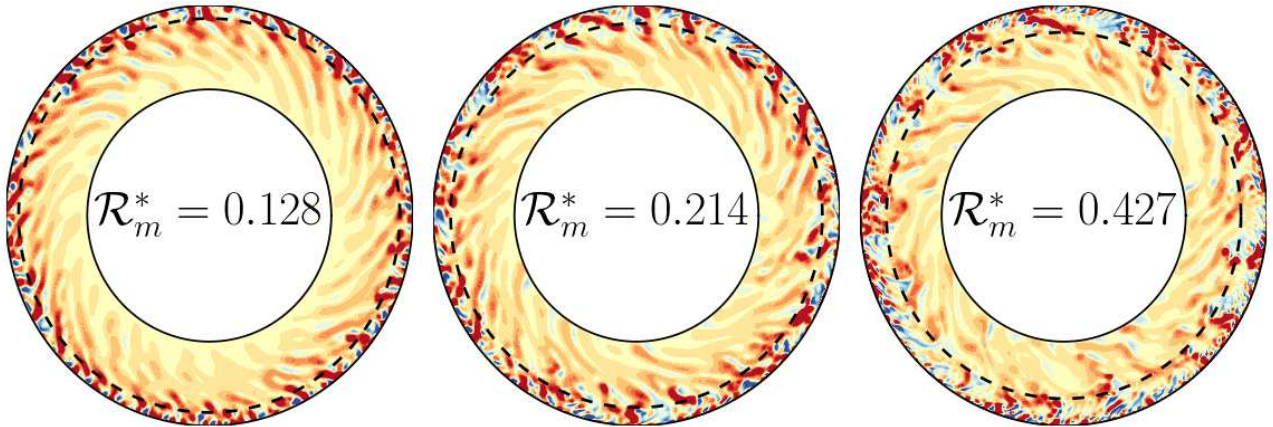
Figure 13: Vorticity along the axis of rotation $\omega_z = (\nabla \times \boldsymbol{u})_z$ displayed in the equatorial plane for three numerical models with $N_\rho = 5$ and $E = 3 \times 10^{-4}$. Red (blue) correspond to positive (negative) values. The dashed black circles correspond to r_{mix} values defined in Fig. 11.
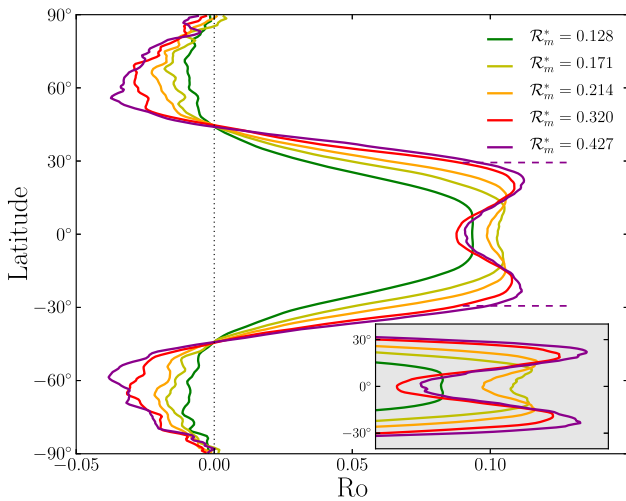
Figure 14: Time-averaged surface zonal flows as a function of latitude for various numerical simulations with $N_\rho = 5$ and $E = 3 \times 10^{-4}$. The corresponding $\mathcal{R}^*(r)$ profiles are given in Fig. 11. The two magenta lines correspond to the theoretical width of the dimple obtained from Eq. (24) for the $\mathcal{R}_m^* = 0.427$ case.
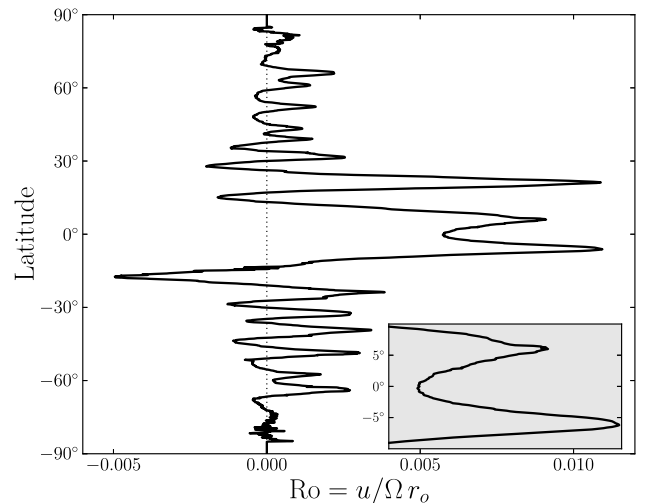
Figure 15: Observed surface zonal winds on Jupiter. Velocities are given in Rossby number units. The data are adapted from Porco et al. (2003) and Vasavada and Showman (2005).

Gastine and Wicht (2012)[1], which relates the modified Nusselt number to the flux-based Rayleigh number $\mathrm{Ra}_q^* = \alpha g q / \rho c_p \Omega^3 d^2$ via $\mathrm{Nu}^* = 0.076 \, \mathrm{Ra}_q^{*0.53}$. $\mathcal{R}_{\mathrm{surf}}^*$ can then directly be obtained with $\mathcal{R}_{\mathrm{surf}}^* = \mathrm{Ra}_q^* / \mathrm{Nu}^*$. Taking an internal heat flux of $5.5\,\mathrm{W.m}^{-2}$, $\alpha = 6 \times 10^{-3}\,\mathrm{K}^{-1}$, $\Omega = 1.75 \times 10^{-4}\,\mathrm{s}^{-1}$, $c_p = 1.2 \times 10^4\,\mathrm{J.kg}^{-1}\mathrm{K}^{-1}$, a gravity $g = 25\,\mathrm{m.s}^{-2}$, a density $\rho = 0.2\,\mathrm{kg.m}^{-3}$ and a lengthscale $d = 0.04\,r_{\mathrm{jup}} = 2.8 \times 10^6\,\mathrm{m}$ (values taken from French et al., 2012), we derive a surface value $\mathcal{R}_{\mathrm{surf}}^* \sim 5 \times 10^{-2}$.

The observed near-surface shear layer on the Sun is also thought to be due to a similar dynamical transition when $\mathcal{R}^*$ crosses unity (see Miesch and Hindman, 2011). As suggested by these authors, another way to evaluate the impact of rotation on convection from observable quantities is to estimate the surface convective Rossby number using $\mathrm{Ro}_c = (\Omega \, \tau_c)^{-1}$, where τ_c is the convective turnover time (see also section 4.2 in Gastine and Wicht, 2012). Using $\tau_c = H_\rho / u_{\mathrm{conv}}$ with $H_\rho \sim 5 \times 10^4\,\mathrm{m}$ from the models by Nettelmann et al. (2012a) and $u_{\mathrm{conv}} \sim 5\,\mathrm{m.s}^{-1}$ from observations by Salyk et al. (2006), we obtain $\tau_c \sim 10^4\,s$, which leads to $\mathrm{Ro}_c \sim 0.5$ (i.e. $\mathcal{R}_{\mathrm{surf}}^* \sim (\mathrm{Ro}_c)^2 \sim 0.25$) at Jupiter's surface, a factor of five larger than the scaling law prediction.

Concerning the uncertainties in our simulations and in our knowledge of Jupiter's dynamics, as well as a possible influence of boundary conditions on scaling laws, this latter value is quite close to the expected value of $\mathcal{R}_{\mathrm{surf}}^* > 1$ required to form a dimple in the transitional regime.

6. Conclusion

We have investigated the transition between the rotation-dominated and the buoyancy-dominated regimes in rotating

---

[1]Note that using $\mathrm{Nu} \sim \mathrm{Ra}^{1/3}$ as suggested by King et al. (2012) leads to very similar values of $\mathcal{R}_{\mathrm{surf}}^*$.

spherical shells with different density contrasts, extending the previous Boussinesq study by Aurnou et al. (2007). Following Gilman and Glatzmaier (1981) and Jones and Kuzanyan (2009), we have employed the anelastic approximation to filter out fast acoustic waves and the related short time steps. Exploring moderate Ekman numbers ($E = 10^{-3} - 3 \times 10^{-4}$) allowed us to raise the Rayleigh number into the buoyancy-dominated regime (characterised here by $\mathcal{R}_m^* > 1$) and to study zonal flows in a broad parameter range. We highlight our main findings:

- When gradually increasing $\mathcal{R}_m^*$, the convective flows change from geostrophic columnar convection when rotation dominates the force balance to three-dimensional turbulent motions when buoyancy becomes significant. In the stratified cases, the latter is characterised by a pronounced asymmetry between broad upwellings and narrow downwellings. This change in the convective features is accompanied by a sharp transition in the zonal flow regime. The equatorial zonal jet reverses its direction at $\mathcal{R}_m^* \simeq 1$, independently of the background density contrast and the Ekman number.

- In the rotation-dominated regime (i.e. $\mathcal{R}_m^* \ll 1$), a combination of quasi-geostrophic columns, density stratification effects, and boundary curvature lead to Reynolds stresses (i.e. the correlation between the cylindrically radial and the azimuthal components of the convective flow) that maintain a prograde equatorial zonal flow. The zonal flow amplitude is relatively independent of the density stratification (see also Gastine and Wicht, 2012).

- In the buoyancy-dominated regime (i.e. $\mathcal{R}_m^* \gg 1$), convection homogenises the angular momentum per unit of mass which leads to a strong retrograde equatorial zonal flow flanked by prograde winds at higher latitudes. The maximum zonal flow amplitude now increases with density stratification. As already mentioned by Aurnou et al. (2007), these zonal flow patterns are reminiscent to those observed on Uranus and Neptune, though it remains uncertain whether convective driving in the ice giants indeed reaches $\mathcal{R}_m^* > 1$.

- Our simulations suggest the possible existence of a third regime where the mean zonal flows are negligible and three dimensional turbulent convection strongly dominates. The timescale of the small-scale convective motions is much shorter than the rotation period which therefore cease to play a role in organising large-scale flow. The transition to the third regime seems to depend on the density stratification and has not been reached for $N_\rho \geq 3$.

- For strongly stratified models in the $\mathcal{R}_m^* \simeq 0.1 - 0.5$ range, both the dynamical regimes I and II can be present in the spherical shell. Close to the outer boundary, buoyancy dominates and leads to more turbulent flows within a thin outer layer. In the deep interior, rotation still dominates, and columnar convection drive the typical zonal flow structure. The turbulent outer layer reduces the zonal

flow amplitude in the center of the equatorial jet. This leads to a dimple similar to the one observed on Jupiter. Its width suggests that a transition between the two dynamical regimes may occur at a depth of 500 km below the 1 bar level in Jupiter. Estimate based on the turnover timescale of convection suggests $\mathcal{R}_{\mathrm{surf}}^* \sim 0.25$, just on the low side of the required value.

- This parameter study on the different zonal flows regimes in rotating anelastic spherical shells has also some possible stellar applications as it helps to clarify the transition between the solar-like differential rotation (i.e. prograde) and the so-called *anti-solar* differential rotation (i.e. retrograde) observed in a number of stellar convection zone models (e.g. Brun and Toomre, 2002; Miesch, 2005; Bessolaz and Brun, 2011; Käpylä et al., 2011a).

Acknowledgements

References

Augustson, K.C., Brown, B.P., Brun, A.S., Miesch, M.S., Toomre, J., 2012. Convection and Differential Rotation in F-type Stars. ApJ 756, 169.

Aurnou, J., Heimpel, M., Wicht, J., 2007. The effects of vigorous mixing in a convective model of zonal flow on the ice giants. Icarus 190, 110–126.

Aurnou, J.M., Heimpel, M.H., 2004. Zonal jets in rotating convection with mixed mechanical boundary conditions. Icarus 169, 492–498.

Ballot, J., Brun, A.S., Turck-Chièze, S., 2007. Simulations of turbulent convection in rotating young solarlike stars: differential rotation and meridional circulation. ApJ 669, 1190–1208.

Bessolaz, N., Brun, A.S., 2011. Hunting for Giant Cells in Deep Stellar Convective Zones Using Wavelet Analysis. ApJ 728, 115.

Braginsky, S.I., Roberts, P.H., 1995. Equations governing convection in earth's core and the geodynamo. Geophysical and Astrophysical Fluid Dynamics 79, 1–97.

Brown, B.P., Browning, M.K., Brun, A.S., Miesch, M.S., Toomre, J., 2008. Rapidly Rotating Suns and Active Nests of Convection. ApJ 689, 1354–1372.

Brown, B.P., Vasil, G.M., Zweibel, E.G., 2012. Energy Conservation and Gravity Waves in Sound-proof Treatments of Stellar Interiors. Part I. Anelastic Approximations. ApJ 756, 109.

Brummell, N.H., Hurlburt, N.E., Toomre, J., 1998. Turbulent Compressible Convection with Rotation. II. Mean Flows and Differential Rotation. ApJ 493, 955.

Brun, A.S., Miesch, M.S., Toomre, J., 2011. Modeling the Dynamical Coupling of Solar Convection with the Radiative Interior. ApJ 742, 79.

Brun, A.S., Toomre, J., 2002. Turbulent Convection under the Influence of Rotation: Sustaining a Strong Differential Rotation. ApJ 570, 865–885.

Busse, F.H., 1983. A model of mean zonal flows in the major planets. Geophysical and Astrophysical Fluid Dynamics 23, 153–174.

Busse, F.H., 1994. Convection driven zonal flows and vortices in the major planets. Chaos 4, 123–134.

Cho, J., Polvani, L.M., 1996. The morphogenesis of bands and zonal winds in the atmospheres on the giant outer planets. Science 273, 335–337.

Christensen, U.R., 2001. Zonal flow driven by deep convection in the major planets. Geophys. Res. Lett. 28, 2553–2556.

Christensen, U.R., 2002. Zonal flow driven by strongly supercritical convection in rotating spherical shells. Journal of Fluid Mechanics 470, 115–133.

Christensen, U.R., Aubert, J., 2006. Scaling properties of convection-driven dynamos in rotating spherical shells and application to planetary magnetic fields. Geophysical Journal International 166, 97–114.

De Rosa, M.L., Gilman, P.A., Toomre, J., 2002. Solar Multiscale Convection and Rotation Gradients Studied in Shallow Spherical Shells. ApJ 581, 1356–1374.

Elliott, J.R., Miesch, M.S., Toomre, J., 2000. Turbulent Solar Convection and Its Coupling with Rotation: The Effect of Prandtl Number and Thermal Boundary Conditions on the Resulting Differential Rotation. ApJ 533, 546–556.

Evonuk, M., Samuel, H., 2012. Simulating rotating fluid bodies: When is vorticity generation via density-stratification important? Earth and Planetary Science Letters 317, 1–7.

French, M., Becker, A., Lorenzen, W., Nettelmann, N., Bethkenhagen, M., Wicht, J., Redmer, R., 2012. Ab Initio Simulations for Material Properties along the Jupiter Adiabat. ApJS 202, 5.

Gastine, T., Wicht, J., 2012. Effects of compressibility on driving zonal flow in gas giants. Icarus 219, 428–442.

Gilman, P.A., 1977. Nonlinear Dynamics of Boussinesq Convection in a Deep Rotating Spherical Shell. I. Geophysical and Astrophysical Fluid Dynamics 8, 93–135.

Gilman, P.A., Foukal, P.V., 1979. Angular velocity gradients in the solar convection zone. ApJ 229, 1179–1185.

Gilman, P.A., Glatzmaier, G.A., 1981. Compressible convection in a rotating spherical shell - I - Anelastic equations. ApJS 45, 335–349.

Glatzmaier, G.A., Gilman, P.A., 1981. Compressible convection in a rotating spherical shell - II - A linear anelastic model. ApJS 45, 351–380.

Glatzmaier, G.A., Gilman, P.A., 1982. Compressible convection in a rotating spherical shell. V - Induced differential rotation and meridional circulation. ApJ 256, 316–330.

Guillot, T., 1999. Interior of Giant Planets Inside and Outside the Solar System. Science 286, 72–77.

Hammel, H.B., de Pater, I., Gibbard, S., Lockwood, G.W., Rages, K., 2005. Uranus in 2003: Zonal winds, banded structure, and discrete features. Icarus 175, 534–545.

Hathaway, D.H., 1982. Nonlinear simulations of solar rotation effects in supergranules. Sol. Phys. 77, 341–356.

Heimpel, M., Aurnou, J., 2007. Turbulent convection in rapidly rotating spherical shells: A model for equatorial and high latitude jets on Jupiter and Saturn. Icarus 187, 540–557.

Heimpel, M., Aurnou, J., Wicht, J., 2005. Simulation of equatorial and high-latitude jets on Jupiter in a deep convection model. Nature 438, 193–196.

Heimpel, M., Gómez Pérez, N., 2011. On the relationship between zonal jets and dynamo action in giant planets. Geophys. Res. Lett. 38, L14201.

Ingersoll, A.P., 1990. Atmospheric dynamics of the outer planets. Science 248, 308–315.

Jones, C.A., Boronski, P., Brun, A.S., Glatzmaier, G.A., Gastine, T., Miesch, M.S., Wicht, J., 2011. Anelastic convection-driven dynamo benchmarks. Icarus 216, 120–135.

Jones, C.A., Kuzanyan, K.M., 2009. Compressible convection in the deep atmospheres of giant planets. Icarus 204, 227–238.

Jones, C.A., Kuzanyan, K.M., Mitchell, R.H., 2009. Linear theory of compressible convection in rapidly rotating spherical shells, using the anelastic approximation. Journal of Fluid Mechanics 634, 291–319.

Julien, K., Knobloch, E., Rubio, A.M., Vasil, G.M., 2012a. Heat Transport in Low-Rossby-Number Rayleigh-Bénard Convection. Phys. Rev. Lett. 109, 254503.

Julien, K., Rubio, A.M., Grooms, I., Knobloch, E., 2012b. Statistical and physical balances in low Rossby number Rayleigh-Bénard convection. Geophysical and Astrophysical Fluid Dynamics 106, 392–428.

Käpylä, P.J., Mantere, M.J., Brandenburg, A., 2011a. Effects of stratification in spherical shell convection. Astronomische Nachrichten 332, 883.

Käpylä, P.J., Mantere, M.J., Guerrero, G., Brandenburg, A., Chatterjee, P., 2011b. Reynolds stress and heat flux in spherical shell convection. A&A 531, A162.

Kaspi, Y., Flierl, G.R., Showman, A.P., 2009. The deep wind structure of the giant planets: Results from an anelastic general circulation model. Icarus 202, 525–542.

King, E.M., Aurnou, J.M., 2012. Thermal evidence for Taylor columns in turbulent rotating Rayleigh-Bénard convection. Phys. Rev. E 85, 016313.

King, E.M., Stellmach, S., Aurnou, J.M., 2012. Heat transfer by rapidly rotating Rayleigh-Bénard convection. Journal of Fluid Mechanics 691, 568–582.

Lantz, S.R., Fan, Y., 1999. Anelastic magnetohydrodynamic equations for modeling solar and stellar convection zones. ApJS 121, 247–264.

Lesieur, M., 1997. Turbulence in Fluids. Kluwer Academic Publishers, Dordrecht, Boston, London.

Lian, Y., Showman, A.P., 2010. Generation of equatorial jets by large-scale latent heating on the giant planets. Icarus 207, 373–393.

Liu, J., Goldreich, P.M., Stevenson, D.J., 2008. Constraints on deep-seated zonal winds inside Jupiter and Saturn. Icarus 196, 653–664.

Liu, J., Schneider, T., 2011. Convective Generation of Equatorial Superrotation in Planetary Atmospheres. Journal of Atmospheric Sciences 68, 2742–2756.

Miesch, M.S., 2005. Large-Scale Dynamics of the Convection Zone and Tachocline. Living Reviews in Solar Physics 2, 1.

Miesch, M.S., Brun, A.S., De Rosa, M.L., Toomre, J., 2008. Structure and Evolution of Giant Cells in Global Models of Solar Convection. ApJ 673, 557–575.

Miesch, M.S., Elliott, J.R., Toomre, J., Clune, T.L., Glatzmaier, G.A., Gilman, P.A., 2000. Three-dimensional Spherical Simulations of Solar Convection. I. Differential Rotation and Pattern Evolution Achieved with Laminar and Turbulent States. ApJ 532, 593–615.

Miesch, M.S., Hindman, B.W., 2011. Gyroscopic Pumping in the Solar Near-surface Shear Layer. ApJ 743, 79.

Nettelmann, N., Becker, A., Holst, B., Redmer, R., 2012a. Jupiter Models with Improved Ab Initio Hydrogen Equation of State (H-REOS.2). ApJ 750, 52.

Nettelmann, N., Helled, R., Fortney, J.J., Redmer, R., 2012b. New indication for a dichotomy in the interior structure of Uranus and Neptune from the application of modified shape and rotation data. Planetary and Space Science in press.

Nettelmann, N., Holst, B., Kietzmann, A., French, M., Redmer, R., Blaschke, D., 2008. Ab Initio equation of state data for Hydrogen, Helium, and water and the internal structure of Jupiter. ApJ 683, 1217–1228.

Plaut, E., Lebranchu, Y., Simitev, R., Busse, F.H., 2008. Reynolds stresses and mean fields generated by pure waves: applications to shear flows and convection in a rotating shell. Journal of Fluid Mechanics 602, 303–326.

Porco, C.C., Baker, E., Barbara, J., Beurle, K., Brahic, A., Burns, J.A., Charnoz, S., Cooper, N., Dawson, D.D., Del Genio, A.D., Denk, T., Dones, L., Dyudina, U., Evans, M.W., Giese, B., Grazier, K., Helfenstein, P., Ingersoll, A.P., Jacobson, R.A., Johnson, T.V., McEwen, A., Murray, C.D., Neukum, G., Owen, W.M., Perry, J., Roatsch, T., Spitale, J., Squyres, S., Thomas, P., Tiscareno, M., Turtle, E., Vasavada, A.R., Veverka, J., Wagner, R., West, R., 2005. Cassini Imaging Science: Initial Results on Saturn's Atmosphere. Science 307, 1243–1247.

Porco, C.C., West, R.A., McEwen, A., Del Genio, A.D., Ingersoll, A.P., Thomas, P., Squyres, S., Dones, L., Murray, C.D., Johnson, T.V., Burns, J.A., Brahic, A., Neukum, G., Veverka, J., Barbara, J.M., Denk, T., Evans, M., Ferrier, J.J., Geissler, P., Helfenstein, P., Roatsch, T., Throop, H., Tiscareno, M., Vasavada, A.R., 2003. Cassini Imaging of Jupiter's Atmosphere, Satellites, and Rings. Science 299, 1541–1547.

Rhines, P.B., 1975. Waves and turbulence on a beta-plane. Journal of Fluid Mechanics 69, 417–443.

Ruediger, G., 1989. Differential rotation and stellar convection. Sun and the solar stars.

Salyk, C., Ingersoll, A.P., Lorre, J., Vasavada, A., Del Genio, A.D., 2006. Interaction between eddies and mean flow in Jupiter's atmosphere: Analysis of Cassini imaging data. Icarus 185, 430–442.

Schaeffer, N., Cardin, P., 2006. Quasi-geostrophic kinematic dynamos at low magnetic Prandtl number. Earth and Planetary Science Letters 245, 595–604.

Schmitz, S., Tilgner, A., 2009. Heat transport in rotating convection without Ekman layers. Phys. Rev. E 80, 015305.

Scott, R.K., Polvani, L.M., 2008. Equatorial superrotation in shallow atmospheres. Geophys. Res. Lett. 35, 24202.

Showman, A.P., Kaspi, Y., Flierl, G.R., 2011. Scaling laws for convection and jet speeds in the giant planets. Icarus 211, 1258–1273.

Soderlund, K.M., King, E.M., Aurnou, J.M. The influence of magnetic fields in planetary dynamo models. Earth and Planetary Science Letters 333, 9–20.

Sromovsky, L.A., Limaye, S.S., Fry, P.M., 1993. Dynamics of Neptune's Major Cloud Features. Icarus 105, 110–141.

Unno, W., Kato, S., Makita, M., 1960. Convective instability in polytropic atmospheres, I. PASJ 12, 192–202.

Vasavada, A.R., Showman, A.P., 2005. Jovian atmospheric dynamics: an up-date after Galileo and Cassini. Reports on Progress in Physics 68, 1935–1996.

Wicht, J., 2002. Inner-core conductivity in numerical dynamo simulations. Physics of the Earth and Planetary Interiors 132, 281–302.

Williams, G.P., 1978. Planetary circulations. I - Barotropic representation of Jovian and terrestrial turbulence. Journal of Atmospheric Sciences 35, 1399–1426.

Zhang, K., 1992. Spiralling columnar convection in rapidly rotating spherical fluid shells. Journal of Fluid Mechanics 236, 535–556.

Zhong, J.Q., Ahlers, G., 2010. Heat transport and the large-scale circulation in rotating turbulent Rayleigh-Bénard convection. Journal of Fluid Mechanics 665, 300–333.

Appendix A. Results table

Table A.4: Results table.

Ekman	N_ρ	$\mathcal{R}_m^*$	Ra/Ra$_c$	Re$_{zon}$	Re$_{mer}$	Re$'$	Ro$_e$	Nu
10^{-3}	0.01	2.92×10^{-2}	1.4	3.2	0.0	5.3	1.85×10^{-3}	1.06
10^{-3}	0.01	4.39×10^{-2}	2.1	7.0	0.1	7.7	3.64×10^{-3}	1.11
10^{-3}	0.01	7.31×10^{-2}	3.5	14.7	0.3	12.6	6.84×10^{-3}	1.21
10^{-3}	0.01	1.17×10^{-1}	5.7	29.3	0.8	20.8	1.62×10^{-2}	1.44
10^{-3}	0.01	1.46×10^{-1}	7.1	43.4	1.1	26.4	2.55×10^{-2}	1.60
10^{-3}	0.01	2.19×10^{-1}	10.6	77.6	3.0	41.6	4.59×10^{-2}	2.18
10^{-3}	0.01	2.92×10^{-1}	14.2	107.5	5.3	57.6	6.32×10^{-2}	2.88
10^{-3}	0.01	4.39×10^{-1}	21.2	145.4	10.7	90.0	8.32×10^{-2}	4.22
10^{-3}	0.01	5.85×10^{-1}	28.3	150.9	11.6	121.1	1.05×10^{-1}	5.36
10^{-3}	0.01	7.31×10^{-1}	35.4	154.1	14.9	149.6	1.08×10^{-1}	6.46
10^{-3}	0.01	8.77×10^{-1}	42.5	140.3	18.1	178.7	1.05×10^{-1}	7.48
10^{-3}	0.01	1.02	49.6	127.8	21.0	205.5	1.01×10^{-1}	8.37
10^{-3}	0.01	1.17	56.6	511.1	51.5	201.5	-3.73×10^{-1}	8.32
10^{-3}	0.01	1.32	63.7	538.2	57.1	215.4	-3.82×10^{-1}	9.16
10^{-3}	0.01	1.46	70.8	561.3	58.6	231.2	-3.85×10^{-1}	9.90
10^{-3}	0.01	2.92	141.6	614.2	94.6	376.6	-4.08×10^{-1}	15.10
10^{-3}	0.01	4.39	212.4	548.8	114.5	483.6	-4.06×10^{-1}	18.70
10^{-3}	0.01	5.85	283.2	471.6	142.8	583.5	-3.88×10^{-1}	21.70
10^{-3}	0.01	7.31	354.0	460.6	153.3	650.5	-3.57×10^{-1}	23.00
10^{-3}	0.01	1.02×10^{1}	495.7	432.1	191.6	802.9	-3.03×10^{-1}	27.00
10^{-3}	0.01	1.46×10^{1}	708.1	351.7	220.9	1010.5	-2.64×10^{-1}	32.10
10^{-3}	0.01	2.92×10^{1}	1416.2	333.4	313.6	1501.5	-1.79×10^{-1}	44.90
10^{-3}	1.00	5.47×10^{-2}	1.2	2.2	0.0	4.5	1.67×10^{-3}	1.04
10^{-3}	1.00	6.25×10^{-2}	1.4	3.8	0.0	5.5	2.72×10^{-3}	1.06
10^{-3}	1.00	9.38×10^{-2}	2.1	11.6	0.1	9.8	8.25×10^{-3}	1.14
10^{-3}	1.00	1.25×10^{-1}	2.7	20.3	0.4	13.0	1.39×10^{-2}	1.23
10^{-3}	1.00	1.56×10^{-1}	3.4	30.1	1.1	16.5	2.31×10^{-2}	1.33
10^{-3}	1.00	2.34×10^{-1}	5.1	58.3	4.5	27.4	3.81×10^{-2}	1.75
10^{-3}	1.00	3.13×10^{-1}	6.9	77.5	9.4	36.8	6.01×10^{-2}	2.22
10^{-3}	1.00	4.69×10^{-1}	10.3	135.4	6.6	78.1	1.07×10^{-1}	3.48
10^{-3}	1.00	6.25×10^{-1}	13.7	160.6	10.0	107.8	1.38×10^{-1}	4.67
10^{-3}	1.00	7.81×10^{-1}	17.1	164.2	13.2	137.9	1.40×10^{-1}	5.75
10^{-3}	1.00	9.38×10^{-1}	20.6	159.7	16.4	165.8	1.31×10^{-1}	6.90
10^{-3}	1.00	1.25	27.4	532.9	61.3	216.7	-4.23×10^{-1}	9.13
10^{-3}	1.00	1.56	34.3	573.4	73.2	255.1	-4.31×10^{-1}	10.80
10^{-3}	1.00	3.13	68.5	636.4	114.2	400.3	-4.32×10^{-1}	16.10
10^{-3}	1.00	4.69	102.8	562.3	140.0	511.0	-4.38×10^{-1}	20.10
10^{-3}	1.00	6.25	137.0	462.6	140.2	584.5	-4.03×10^{-1}	21.80
10^{-3}	1.00	9.38	205.5	514.7	214.5	753.3	-3.89×10^{-1}	28.10
10^{-3}	3.00	7.92×10^{-2}	1.1	1.3	0.0	4.9	2.17×10^{-3}	1.03
10^{-3}	3.00	8.80×10^{-2}	1.2	2.8	0.1	6.2	4.57×10^{-3}	1.05
10^{-3}	3.00	1.32×10^{-1}	1.8	13.8	0.3	12.6	2.04×10^{-2}	1.13
10^{-3}	3.00	1.76×10^{-1}	2.5	27.8	0.5	18.5	3.65×10^{-2}	1.23
10^{-3}	3.00	2.64×10^{-1}	3.7	59.7	2.1	36.0	7.10×10^{-2}	1.67
10^{-3}	3.00	3.52×10^{-1}	4.9	87.3	3.6	51.0	1.04×10^{-1}	2.06
10^{-3}	3.00	4.40×10^{-1}	6.2	110.5	5.1	64.6	1.24×10^{-1}	2.42
10^{-3}	3.00	5.28×10^{-1}	7.4	129.8	6.3	77.3	1.45×10^{-1}	2.74
10^{-3}	3.00	6.16×10^{-1}	8.6	142.8	7.8	90.0	1.59×10^{-1}	3.07
10^{-3}	3.00	7.04×10^{-1}	9.8	153.8	8.7	101.5	1.65×10^{-1}	3.32
10^{-3}	3.00	8.80×10^{-1}	12.3	165.9	10.9	124.7	1.66×10^{-1}	3.87
10^{-3}	3.00	1.14	16.0	459.3	40.6	161.6	-4.40×10^{-1}	5.44
10^{-3}	3.00	1.32	18.5	501.6	50.8	177.7	-4.62×10^{-1}	5.98
10^{-3}	3.00	1.76	24.6	565.5	70.1	217.6	-4.99×10^{-1}	7.19
10^{-3}	3.00	2.64	36.9	633.4	94.7	285.1	-5.18×10^{-1}	9.00
10^{-3}	3.00	3.52	49.2	669.2	110.3	335.3	-5.25×10^{-1}	10.30
10^{-3}	3.00	6.16	86.1	682.3	153.1	441.0	-5.39×10^{-1}	12.20
10^{-3}	3.00	1.76×10^{1}	246.1	753.1	325.1	625.8	-5.41×10^{-1}	13.80
10^{-3}	5.00	4.75×10^{-2}	1.2	1.5	0.1	6.7	3.79×10^{-3}	1.05
10^{-3}	5.00	7.12×10^{-2}	1.8	6.2	0.6	11.5	1.37×10^{-2}	1.11
10^{-3}	5.00	9.49×10^{-2}	2.5	13.5	0.9	18.0	2.67×10^{-2}	1.19
10^{-3}	5.00	1.19×10^{-1}	3.1	21.2	1.6	27.8	3.53×10^{-2}	1.37
10^{-3}	5.00	1.42×10^{-1}	3.7	28.5	2.4	34.8	4.76×10^{-2}	1.49
10^{-3}	5.00	1.66×10^{-1}	4.3	35.9	2.9	40.8	5.70×10^{-2}	1.59
10^{-3}	5.00	1.90×10^{-1}	4.9	42.6	3.1	46.2	6.70×10^{-2}	1.68

Ekman	N_ρ	$\mathcal{R}_m^*$	Ra/Ra$_c$	Re$_{zon}$	Re$_{mer}$	Re$'$	Ro$_e$	Nu
10^{-3}	5.00	2.37×10^{-1}	6.2	54.3	3.6	56.4	7.68×10^{-2}	1.84
10^{-3}	5.00	3.56×10^{-1}	9.2	77.8	5.4	80.1	9.04×10^{-2}	2.24
10^{-3}	5.00	4.75×10^{-1}	12.3	90.5	7.4	102.9	7.82×10^{-2}	2.66
10^{-3}	5.00	5.93×10^{-1}	15.4	84.2	9.7	127.3	4.54×10^{-2}	3.07
10^{-3}	5.00	7.12×10^{-1}	18.5	318.3	24.4	138.3	-3.68×10^{-1}	3.65
10^{-3}	5.00	8.31×10^{-1}	21.6	357.7	27.9	150.1	-3.98×10^{-1}	3.97
10^{-3}	5.00	9.49×10^{-1}	24.6	384.5	31.1	163.1	-4.21×10^{-1}	4.26
10^{-3}	5.00	1.19	30.8	437.4	37.1	184.5	-4.52×10^{-1}	4.77
10^{-3}	5.00	1.42	36.9	476.9	45.0	205.3	-4.80×10^{-1}	5.23
10^{-3}	5.00	2.37	61.6	574.0	68.0	270.5	-5.33×10^{-1}	6.03
10^{-3}	5.00	4.75	123.2	662.8	101.6	370.8	-5.54×10^{-1}	7.08
10^{-3}	5.00	7.12	184.7	701.6	135.6	421.7	-5.66×10^{-1}	7.23
10^{-3}	5.00	1.19×10^{1}	307.9	749.0	188.3	488.4	-5.80×10^{-1}	7.53
3×10^{-4}	0.01	7.89×10^{-3}	1.2	2.1	0.0	4.2	3.04×10^{-4}	1.03
3×10^{-4}	0.01	1.32×10^{-2}	2.0	8.5	0.1	7.9	1.17×10^{-3}	1.07
3×10^{-4}	0.01	2.63×10^{-2}	3.9	25.4	0.3	15.7	3.86×10^{-3}	1.16
3×10^{-4}	0.01	6.58×10^{-2}	9.9	106.3	1.2	39.7	1.84×10^{-2}	1.60
3×10^{-4}	0.01	7.89×10^{-2}	11.8	137.8	1.8	48.6	2.48×10^{-2}	1.82
3×10^{-4}	0.01	1.05×10^{-1}	15.8	200.7	3.3	69.6	3.74×10^{-2}	2.40
3×10^{-4}	0.01	1.32×10^{-1}	19.7	263.3	5.3	90.2	4.84×10^{-2}	2.98
3×10^{-4}	0.01	1.97×10^{-1}	29.6	340.7	10.4	145.1	7.10×10^{-2}	4.59
3×10^{-4}	0.01	2.63×10^{-1}	39.4	404.8	15.9	194.4	8.95×10^{-2}	6.03
3×10^{-4}	0.01	3.95×10^{-1}	59.1	492.5	26.4	282.5	1.09×10^{-1}	8.75
3×10^{-4}	0.01	5.26×10^{-1}	78.8	565.8	36.7	380.0	9.26×10^{-2}	11.70
3×10^{-4}	0.01	7.89×10^{-1}	118.2	615.9	53.3	571.7	6.53×10^{-2}	16.70
3×10^{-4}	0.01	1.05	157.6	2069.2	172.7	550.7	-3.76×10^{-1}	19.00
3×10^{-4}	0.01	1.32	197.0	2172.9	181.4	656.9	-4.11×10^{-1}	22.60
3×10^{-4}	0.01	2.63	394.1	2151.6	232.4	1093.1	-4.25×10^{-1}	35.90
3×10^{-4}	1.00	2.11×10^{-2}	1.2	2.7	0.0	4.7	5.35×10^{-4}	1.02
3×10^{-4}	1.00	2.81×10^{-2}	1.5	8.9	0.0	8.2	1.73×10^{-3}	1.06
3×10^{-4}	1.00	4.22×10^{-2}	2.3	25.6	0.1	14.1	5.26×10^{-3}	1.13
3×10^{-4}	1.00	5.63×10^{-2}	3.1	49.9	0.4	22.6	1.06×10^{-2}	1.23
3×10^{-4}	1.00	8.44×10^{-2}	4.6	105.8	1.2	39.0	2.55×10^{-2}	1.51
3×10^{-4}	1.00	1.13×10^{-1}	6.2	162.3	2.4	57.1	4.04×10^{-2}	1.91
3×10^{-4}	1.00	1.41×10^{-1}	7.7	210.4	3.9	75.4	5.07×10^{-2}	2.36
3×10^{-4}	1.00	2.11×10^{-1}	11.6	302.5	8.8	125.7	7.39×10^{-2}	3.70
3×10^{-4}	1.00	2.81×10^{-1}	15.5	379.2	13.4	173.1	1.02×10^{-1}	5.09
3×10^{-4}	1.00	5.63×10^{-1}	31.0	592.1	32.7	340.6	1.35×10^{-1}	10.20
3×10^{-4}	1.00	8.44×10^{-1}	46.5	672.2	52.9	556.8	4.46×10^{-2}	16.90
3×10^{-4}	1.00	1.13	62.0	2088.3	145.0	614.0	-3.47×10^{-1}	23.10
3×10^{-4}	3.00	3.17×10^{-2}	1.1	1.2	0.0	4.8	7.32×10^{-4}	1.02
3×10^{-4}	3.00	4.75×10^{-2}	1.6	15.1	0.2	12.6	6.80×10^{-3}	1.08
3×10^{-4}	3.00	6.33×10^{-2}	2.2	40.8	0.4	21.2	1.73×10^{-2}	1.17
3×10^{-4}	3.00	7.92×10^{-2}	2.7	72.6	0.7	30.0	3.00×10^{-2}	1.27
3×10^{-4}	3.00	1.19×10^{-1}	4.0	152.3	2.8	60.1	5.84×10^{-2}	1.82
3×10^{-4}	3.00	1.58×10^{-1}	5.4	227.9	5.3	89.1	8.23×10^{-2}	2.44
3×10^{-4}	3.00	2.38×10^{-1}	8.1	363.9	9.7	140.9	1.27×10^{-1}	3.60
3×10^{-4}	3.00	3.17×10^{-1}	10.8	469.4	13.7	187.3	1.58×10^{-1}	4.66
3×10^{-4}	3.00	4.75×10^{-1}	16.2	572.5	21.4	275.8	1.83×10^{-1}	6.76
3×10^{-4}	3.00	6.33×10^{-1}	21.5	601.7	28.9	354.1	1.52×10^{-1}	8.04
3×10^{-4}	3.00	7.92×10^{-1}	26.9	513.6	40.1	492.3	2.86×10^{-1}	10.60
3×10^{-4}	3.00	1.19	40.4	2038.5	158.1	518.3	-5.13×10^{-1}	16.90
3×10^{-4}	5.00	1.50×10^{-2}	1.1	0.8	0.0	5.8	8.20×10^{-4}	1.03
3×10^{-4}	5.00	2.14×10^{-2}	1.6	6.6	0.1	11.5	5.45×10^{-3}	1.06
3×10^{-4}	5.00	3.20×10^{-2}	2.4	21.3	0.7	21.3	1.54×10^{-2}	1.16
3×10^{-4}	5.00	4.27×10^{-2}	3.1	41.4	1.6	34.8	2.60×10^{-2}	1.35
3×10^{-4}	5.00	6.41×10^{-2}	4.7	93.8	3.5	72.1	4.73×10^{-2}	2.00
3×10^{-4}	5.00	8.54×10^{-2}	6.3	149.9	4.9	98.1	6.71×10^{-2}	2.46
3×10^{-4}	5.00	1.28×10^{-1}	9.4	249.5	8.2	144.8	9.68×10^{-2}	3.27
3×10^{-4}	5.00	1.71×10^{-1}	12.6	323.5	11.5	185.3	1.05×10^{-1}	3.96
3×10^{-4}	5.00	2.14×10^{-1}	15.7	372.0	15.0	224.7	9.74×10^{-2}	4.67
3×10^{-4}	5.00	3.20×10^{-1}	23.5	448.5	20.2	295.7	8.78×10^{-2}	5.53
3×10^{-4}	5.00	4.27×10^{-1}	31.4	470.8	26.2	361.0	9.09×10^{-2}	6.69
3×10^{-4}	5.00	6.41×10^{-1}	47.1	477.2	35.6	454.6	7.71×10^{-2}	8.75

Table A.4: Continued.

Ekman	N_ρ	$\mathcal{R}_m^*$	Ra/Ra$_c$	Re$_{zon}$	Re$_{mer}$	Re$'$	Ro$_e$	Nu
3×10^{-4}	5.00	8.54×10^{-1}	62.8	1550.8	121.8	435.8	-4.76×10^{-1}	9.92

Ekman	N_ρ	$\mathcal{R}_m^*$	Ra/Ra$_c$	Re$_{zon}$	Re$_{mer}$	Re$'$	Ro$_e$	Nu
3×10^{-4}	5.00	8.54×10^{-1}	62.8	1550.8	121.8	435.8	-4.76×10^{-1}	9.92